

Parabolic approach to optimal perturbations in compressible boundary layers

By SIMONE ZUCCHER¹, ANATOLI TUMIN¹
AND ELI RESHOTKO²

¹Aerospace and Mechanical Engineering Department, University of Arizona, PO Box 210119,
Tucson, AZ 85721-00119, USA

²Case Western Reserve University, Cleveland, OH 44106, USA

(Received 27 April 2005 and in revised form 4 November 2005)

Optimal perturbations in compressible, non-parallel boundary layers are considered here. The flows past a flat plate and past a sphere are analysed. The governing equations are derived from the linearized Navier–Stokes equations by employing a scaling that relies on the presence of streamwise vortices, which are well-known for being responsible for the ‘lift-up’ effect. Consequently, the energy norm of the inlet perturbation encompasses the wall-normal and spanwise velocity components only. The effect of different choices of the energy norm at the outlet is studied, testing full (all velocity components and temperature) and partial (streamwise velocity and temperature only) norms. Optimal perturbations are computed via an iterative algorithm completely derived in the discrete framework. The latter simplifies the derivation of the adjoint equations and the coupling conditions at the inlet and outlet.

Results for the flat plate show that when the Reynolds number is of the order of 10^3 , a significant difference in the energy growth is found between the cases of full and partial energy norms at the outlet. The effect of the wall temperature is in agreement with previous parallel-flow results, with cooling being a destabilizing factor for both flat plate and sphere. Flow divergence, which characterizes the boundary layer past the sphere, has significant effects on the transient growth phenomenon. In particular, an increase of the sphere radius leads to a larger transient growth, with stronger effects in the vicinity of the stagnation point. In the range of interesting values of the Reynolds number that are typical of wind tunnel tests and flight conditions for a sphere, no significant role is played by the wall-normal and streamwise velocity components at the outlet.

1. Introduction

The problem of optimal disturbances, in the context of bypass transition to turbulence, has been of great interest during the last decade. This interest is motivated by the fact that there are many applications where transition to turbulence occurs without the classical exponential growth, allowing a large transient growth of the disturbance energy in flows that are stable to wave-like perturbations (Tollmien–Schlichting waves).

Today it is clear that transient growth arises from the coupling between slightly damped, highly oblique Orr–Sommerfeld (OS) and Squire modes. This can lead to an algebraic growth followed, in viscous flows, by exponential decay in subcritical

regions outside the Tollmien–Schlichting (TS) neutral curve. A weak transient growth can also occur for two-dimensional modes since the OS operator and its compressible counterpart are not self-adjoint, and therefore their eigenfunctions are not strictly orthogonal (Reshotko 2001; Schmid & Henningson 2001).

Historically, the first approach to non-modal disturbances was in the inviscid limit. Ellingsen & Palm (1975) found that the streamwise disturbance velocity amplitude may grow algebraically in time, even though the basic flow does not possess an inflection point. This growth mechanism was labelled ‘lift-up’ (Landahl 1975). Later on, Landahl (1980) showed that all parallel inviscid shear flows are unstable to a wide class of three-dimensional disturbances and the result is independent of whether or not the shear flow is unstable to exponential growth. The temporal analysis involving resonance between OS and Squire modes was employed for the study of Couette flow (Gustavsson & Hultgren 1980), Poiseuille flow (Gustavsson 1981) and boundary layers (Hultgren & Gustavsson 1981; Benney & Gustavsson 1981; Jang, Benney & Gran 1986), revealing a viscous decay following initial algebraic growth of the disturbance, otherwise known as transient growth. Meanwhile, the transient growth phenomenon was intensively studied in meteorology (Farrell 1982, 1984, 1986, 1987).

Farrell (1988*a, b*) was the first to use the term optimal perturbations to denote the initial flow disturbances that produced the maximum gain, defined as the ratio between the perturbation kinetic energies at the final and initial time. A similar concept had, however, already been introduced for flow in a pipe by Boberg & Brosa (1988). The first quantitative calculation of three-dimensional optimal perturbations with respect to temporal growth for a parallel approximation of the Blasius boundary layer was performed by Butler & Farrell (1992). Other work (Gustavsson 1991; Reddy & Henningson 1993; Trefethen *et al.* 1993), carried out more than a decade ago, recognized the great potential of non-modal growth for explaining bypass transition.

Optimal perturbations in the spatial framework have only more recently been considered. The spatial Cauchy problem within the scope of the linearized Navier–Stokes equations is, however, radically different from the temporal one and is ill-posed. This is the main obstacle to applying to the spatial analysis the same optimization methods used in the temporal case. The problem arises from the presence of modes with a negative imaginary part of the streamwise wavenumber α . These are modes decaying upstream and associated with the downstream boundary conditions. Tumin & Reshotko (2001) pointed out that if the downstream boundary is moved far away, the upstream decaying modes can be neglected and the optimization can be carried out within the scope of the Cauchy problem, similarly to the temporal analysis. The ill-posedness of the spatial Cauchy problem was first overcome by considering the (linearized) boundary layer equations (Andersson, Berggren & Henningson 1999; Luchini 2000) instead of the Navier–Stokes equations. In addition, Andersson *et al.* (1999) and Luchini (2000) included non-parallel effects. It was found that the optimal initial disturbance is composed of stationary streamwise vortices whereas the induced velocity field is dominated by streamwise streaks. For example, in the case of an incompressible boundary layer past a flat plate, the maximum amplification occurs in the steady case (frequency $\omega = 0$) and for a non-zero value of the spanwise wavenumber $\beta = 0.45$ (scaled with $l = \sqrt{\nu L/U_\infty}$, ν being the kinematic viscosity, U_∞ the free-stream velocity and L the longitudinal distance from the leading edge to the location where output energy is maximized). For the spatial problem, Zuccher, Bottaro & Luchini (2006) computed the optimal perturbations in the nonlinear case.

The compressible counterpart of the aforementioned works has also been considered. Temporal (Hanifi, Schmidt & Henningson 1996; Hanifi & Henningson

1998) and spatial (Reshotko & Tumin 2000; Tumin & Reshotko 2001, 2004) analyses of the transient growth phenomenon have been carried out within the scope of the parallel-flow approximation. Tumin & Reshotko (2003) developed a model for transient growth including non-parallel effects in the compressible boundary layer past a flat plate.

Compressible optimal perturbations calculated by including surface curvature effects and non-parallel growth of the boundary layer do not exist and could be of great importance to explain the long-standing blunt-body paradox (Reshotko & Tumin 2000).

Depending on the choice of the norm, which states what quantity will be maximized, constrained optimization in the framework of optimal perturbations can lead to quite different results. With reference to the incompressible case, Andersson *et al.* (1999) maximized a full energy norm including all velocity components, whereas Luchini (2000) considered the energy of the streamwise component only. On the other hand, the choice of the initial condition (i.e. the choice of the norm at the inlet) may also contribute to the result. In the incompressible framework, the full inlet energy norm (Andersson *et al.* 1999) and the energy norm including only the spanwise and wall-normal velocity components (Luchini 2000) have been employed. In Andersson *et al.* (1999) both norms at the inlet and at the outlet depend on the Reynolds number Re . However, in the limit $Re \rightarrow \infty$ (in practice for $Re > 10^4$) results collapse onto those obtained by Luchini (2000).

The choice of the energy norm, therefore, can be a delicate issue, especially in the compressible case where effects due to compressibility should be taken into account through the inclusion of density and temperature fluctuations. The physics of transient growth is mainly dominated by streamwise vortices (Andersson *et al.* 1999; Luchini 2000) and therefore the choice of an initial energy excluding the streamwise velocity component, in the fashion proposed by Luchini (2000), is satisfactory. The choice of an outlet norm including only temperature and the component of the velocity in the streamwise direction, however, might not represent completely the structure of the flow field if the flow is not dominated by streamwise streaks. This could be the case for a blunt body, for which there are some indications that the largest transient growth is located close to the stagnation point (Reshotko & Tumin 2004). Due to the short interval in the streamwise direction, a flow field mainly dominated by streaks might not be completely established and thus the contribution of the wall-normal and spanwise velocity components to the energy norm at the outlet could be non-negligible.

The objective of the present work is therefore twofold. In the framework of compressible optimal perturbations, the use of a full energy norm at the outlet (FENO) is considered and compared with the use of a partial energy norm. Curvature effects are included in order to investigate optimal disturbances developing in the compressible, non-parallel boundary layer over a sphere.

2. Governing equations

Governing equations for the steady, three-dimensional disturbance in a compressible flow are derived from the linearized Navier–Stokes equations.

A small parameter $\epsilon = H_{\text{ref}}/L_{\text{ref}}$ is introduced for scaling purposes, where $H_{\text{ref}} = \sqrt{\nu_{\text{ref}} L_{\text{ref}}/U_{\text{ref}}}$ is a typical boundary layer length in the wall-normal direction y and L_{ref} is a typical scale of the geometry (length of the flat plate L , radius of the sphere R , etc.), U_{ref} and ν_{ref} are respectively the reference scaling velocity and

kinematic viscosity. In the case of the flat plate $H_{\text{ref}} = l = \sqrt{\nu_{\infty} L / U_{\infty}}$ (the subscript ∞ denotes free-stream parameters, outside the boundary layer), while for the sphere $H_{\text{ref}} = \sqrt{\nu_{\text{ref}} R / U_{\text{ref}}}$ where the reference quantities are the values at the edge of the boundary layer at a certain downstream location x_{ref} , x being the streamwise direction. The scaling parameter ϵ is thus strictly related to the Reynolds number Re . For the flat plate $\epsilon = Re^{-1/2}$, where $Re = U_{\infty} L / \nu_{\infty}$ is the Reynolds number based on the length of the plate and free-stream conditions, while for the sphere $\epsilon = Re_{\text{ref}}^{-1/2}$, where $Re_{\text{ref}} = U_{\text{ref}} R / \nu_{\text{ref}}$ is the reference Reynolds number based on the radius of the sphere R and reference parameters.

It follows from previous works regarding optimal perturbations in both incompressible and compressible boundary layers (Luchini 2000; Cathalifaud & Luchini 2000; Tumin & Reshotko 2004; Zuccher, Luchini & Bottaro 2004; Zuccher *et al.* 2006), that the disturbance flow is expected to be dominated by streamwise vortices and therefore the following scaling is employed. The streamwise coordinate x is normalized with L_{ref} , whereas the wall-normal coordinate y and the spanwise coordinate z are scaled with ϵL_{ref} . The streamwise velocity component u is scaled with U_{ref} , wall-normal velocity v and spanwise velocity w with ϵU_{ref} , temperature T with T_{ref} and pressure p with $\epsilon^2 \rho_{\text{ref}} U_{\text{ref}}^2$. Density ρ is eliminated through the state equation.

Due to the scaling adopted, the second derivative with respect to the streamwise coordinate x is smaller than the other terms, and is therefore neglected. This leads to a change in the nature of the equations from elliptic (Navier–Stokes equations) to parabolic.

For the flat plate, perturbations are assumed to be periodic in z , so that a general variable can be expressed as $q(x, y) \exp(i\beta z)$, where $q(x, y)$ is the amplitude, which depends on x and y , β is the spanwise wavenumber and i is the imaginary unit. Similarly, for the sphere, perturbations are assumed to be periodic in the azimuthal direction ϕ , proportional to $\exp(im\phi)$, where m is the azimuthal index.

If the vector of perturbations is $\mathbf{f} = [u, v, w, T, p]^T$ (where the superscript T denotes the transpose), and $w = i\tilde{w}$ (\tilde{w} being the amplitude of the spanwise velocity component), the governing equations can be written as follows (Tumin & Reshotko 2003):

$$(\mathbf{A}\mathbf{f})_x = (\mathbf{D}\mathbf{f}_y)_x + \mathbf{B}_0\mathbf{f} + \mathbf{B}_1\mathbf{f}_y + \mathbf{B}_2\mathbf{f}_{yy}. \quad (2.1)$$

This form of the governing equations is general and can be derived for different geometries such as flat plate, sphere, sharp cone or blunt-nose cone. Non-zero elements of the 5×5 real matrices \mathbf{A} , \mathbf{B}_0 , \mathbf{B}_1 , \mathbf{B}_2 and \mathbf{D} for the flat plate are defined in the appendix of Tumin & Reshotko (2003), while for the sphere they are given in the Appendix.

As far as boundary conditions are concerned, all perturbations are required to be zero at the wall except for p , while in the free stream all perturbations vanish except for v :

$$\left. \begin{array}{l} y = 0 : \quad u = 0; \quad v = 0; \quad w = 0; \quad T = 0 \\ y \rightarrow \infty : \quad u \rightarrow 0; \quad w \rightarrow 0; \quad p \rightarrow 0; \quad T \rightarrow 0. \end{array} \right\} \quad (2.2)$$

In order to isolate the derivative with respect to x , system (2.1) can be recast in a simple form as

$$(\mathbf{H}_1\mathbf{f})_x + \mathbf{H}_2\mathbf{f} = 0 \quad (2.3)$$

where operators \mathbf{H}_1 and \mathbf{H}_2 are still 5×5 real matrices and contain the dependence on x and y due to the basic flow:

$$\mathbf{H}_1 = \mathbf{A} - \mathbf{D}(\cdot)_y, \quad \mathbf{H}_2 = -\mathbf{B}_0 - \mathbf{B}_1(\cdot)_y - \mathbf{B}_2(\cdot)_{yy}. \quad (2.4)$$

System (2.3) is parabolic in nature and can be solved by means of a downstream marching procedure with initial data specified at the inlet section of the domain $x = x_{\text{in}}$.

It is worth noting that, due to the normalization chosen, the disturbance equations for the flat plate are Reynolds-number independent, i.e. the Reynolds number Re does not enter explicitly in the equations, while for the sphere they are not Reynolds-number independent due to the parameter ϵ in the scaling, which is associated with curvature effects.

3. Constrained optimization and adjoint discrete equations

As stated in the Introduction, we are interested in finding initial optimal disturbances for the compressible boundary layer over a flat plate and a sphere. The term ‘optimal’ here refers to the initial condition that produces the worst possible scenario as far as transition is concerned. It is clear that the choice of a specific quantity that can measure this worst case is neither easy nor unique. In previous works dealing with optimal perturbations in the incompressible framework (Andersson *et al.* 1999; Luchini 2000; Cathalifaud & Luchini 2000; Zuccher *et al.* 2004, 2006), the kinetic energy of the disturbance field has always been the choice.

Once the objective function has been identified, the Lagrangian multiplier technique is employed in order to solve the constrained optimization problem. In doing so the costate (or adjoint) equations are derived. If this is applied to the discrete equations, the discrete version of the adjoint problem is obtained.

3.1. The objective function

In problems related to boundary-layer transition, the quantity that monitors the instability development is typically the kinetic energy. In optimal perturbation studies it is usually maximized at the outlet of the computational domain, but in other cases the integral of the kinetic energy over the whole domain has been considered, especially for optimal control problems (see Cathalifaud & Luchini 2000; Zuccher *et al.* 2004). Since one of the goals of the present study is to check how the use of a ‘full energy norm’ at the outlet can influence the results, the expression we choose to maximize is Mack’s energy norm (Mack 1969) including the perturbation kinetic energy density and temperature fluctuations in the outlet plane. After employing the scaling in § 2, it is written

$$E_{\text{out}} = \int_0^\infty \left[\rho_{s,\text{out}} (u_{\text{out}}^2 + \epsilon^2 (v_{\text{out}}^2 + w_{\text{out}}^2)) + \frac{\rho_{\text{out}}^2 T_{s,\text{out}}}{\gamma \rho_{s,\text{out}} M^2} + \frac{T_{\text{out}}^2 \rho_{s,\text{out}}}{\gamma (\gamma - 1) T_{s,\text{out}} M^2} \right] dy. \quad (3.1)$$

Expression (3.1) was derived for perturbations in the boundary layer over a flat plate within the temporal framework and is here utilized for the spatial one, as done by Tumin & Reshotko (2003) (for the sphere, the integration generates a slightly different expression for the energy norm, which can be found in the Appendix). After employing the equation of state for the basic flow and for the perturbation, the norm becomes

$$E_{\text{out}} = \int_0^\infty \left[\rho_{s,\text{out}} (u_{\text{out}}^2 + \epsilon^2 (v_{\text{out}}^2 + w_{\text{out}}^2)) + \frac{p_{s,\text{out}} T_{\text{out}}^2}{(\gamma - 1) T_{s,\text{out}}^2 M^2} \right] dy \quad (3.2)$$

and can be more compactly recast in matrix form as

$$E_{\text{out}} = \int_0^\infty (\mathbf{f}_{\text{out}}^T \tilde{\mathbf{M}}_{\text{out}} \mathbf{f}_{\text{out}}) dy \quad (3.3)$$

where the linear operator $\tilde{\mathbf{M}}_{\text{out}}$ is a diagonal 5×5 matrix

$$\tilde{\mathbf{M}}_{\text{out}} = \begin{bmatrix} \rho_{s\text{out}} & 0 & 0 & 0 & 0 \\ 0 & \epsilon^2 \rho_{s\text{out}} & 0 & 0 & 0 \\ 0 & 0 & \epsilon^2 \rho_{s\text{out}} & 0 & 0 \\ 0 & 0 & 0 & \frac{p_{s\text{out}}}{(\gamma - 1)T_{s\text{out}}^2 M^2} & 0 \\ 0 & 0 & 0 & 0 & 0 \end{bmatrix}. \quad (3.4)$$

The initial condition for the compressible boundary-layer equations is not arbitrary, but only three of the five variables can be imposed at x_{in} (Ting 1965). However, in the incompressible case and for $Re \rightarrow \infty$, Luchini (2000) observed that the choice $u_{\text{in}} = 0$, $p_{\text{in}} = 0$, v_{in} and w_{in} related by the continuity equation, guarantees the maximum gain in an input–output fashion (in the incompressible case the number of independent initial conditions is two; see also Luchini & Bottaro (1998), Luchini (2000) and Zuccher *et al.* (2006)). This choice also corresponds to the physical mechanism, observed in transitional boundary layer flows, known as the lift-up effect (Landahl 1980), according to which streamwise vortices lift low-momentum flow up (from the wall) and push down high-momentum flow causing streaks that eventually break down to turbulence. Led by these considerations, here we focus on initial perturbations with only v and w non-zero, which correspond to steady, streamwise vortices. It should be noticed, however, that in the case of finite Reynolds number, for example $Re = 1000$, and for the incompressible boundary layer past a flat plate, the choice of a full energy norm at both inlet and outlet guarantees the largest gain in the optimization (Andersson *et al.* 1999).

The kinetic energy of the optimal disturbance f_{in} , if only v_{in} and w_{in} are non-zero, is therefore

$$E_{\text{in}} = \int_0^\infty [\rho_{s\text{in}} \epsilon^2 (v_{\text{in}}^2 + w_{\text{in}}^2)] dy, \quad (3.5)$$

or more compactly

$$E_{\text{in}} = \int_0^\infty (f_{\text{in}}^T \tilde{\mathbf{M}}_{\text{in}} f_{\text{in}}) dy \quad (3.6)$$

where $\tilde{\mathbf{M}}_{\text{in}}$ is a 5×5 diagonal matrix

$$\tilde{\mathbf{M}}_{\text{in}} = \begin{bmatrix} 0 & 0 & 0 & 0 & 0 \\ 0 & \epsilon^2 \rho_{s\text{in}} & 0 & 0 & 0 \\ 0 & 0 & \epsilon^2 \rho_{s\text{in}} & 0 & 0 \\ 0 & 0 & 0 & 0 & 0 \\ 0 & 0 & 0 & 0 & 0 \end{bmatrix}. \quad (3.7)$$

The quantity to be maximized is $G = E_{\text{out}}/E_{\text{in}}$, the ratio between the outlet and inlet norms. However, in order to allow direct comparison with previous works, $G\epsilon^2$ will be presented in the results section. Combining expressions (3.2) and (3.5) leads

to

$$G\epsilon^2 = \frac{\int_0^\infty \left[\rho_{s\text{out}} (u_{\text{out}}^2 + \epsilon^2 (v_{\text{out}}^2 + w_{\text{out}}^2)) + \frac{p_{s\text{out}} T_{\text{out}}^2}{(\gamma - 1) T_{s\text{out}}^2 M^2} \right] dy}{\int_0^\infty [\rho_{s\text{in}} (v_{\text{in}}^2 + w_{\text{in}}^2)] dy}, \quad (3.8)$$

which reduces, in the $Re \rightarrow \infty$ limit ($\epsilon \rightarrow 0$), to the expression maximized by Tumin & Reshotko (2003) for the compressible case and by Luchini (2000) for the incompressible one. Since the problem is linear, an arbitrary normalization for the initial disturbance at x_{in} can be chosen, e.g. $E_{\text{in}} = E_0 = 1$, so that the maximization of (3.8) turns out to be equivalent to the maximization of expression (3.3).

From the above discussion it is clear that the whole problem of finding optimal perturbations reduces to a ‘constrained optimization’, in which we seek the initial conditions for the disturbance equations (2.3) that maximize (3.3) and that satisfy the constraint $E_{\text{in}} = E_0$ at x_{in} together with the direct equations (2.3) and boundary conditions (2.2) at each $x \in (x_{\text{in}}; x_{\text{out}})$.

3.2. Constrained optimization

The classical Lagrange multiplier technique is one of the best known tools to solve constrained optimization problems. As applied to optimal perturbations, numerous examples can be found in the literature regarding the continuous version of such an approach, which leads to the so-called adjoint equations in a continuous fashion. Rigorously speaking, in the theory of linear operators the adjoint equations are derived by satisfying an equality involving an inner product (Naylor & Sell 2000; Kreyszig 1989). Therefore their form is not necessarily related to constrained optimization problems. On the other hand, when the adjoint equations are derived from a constrained optimization (as in our case), only if the objective function includes exclusively quantities at the boundaries of the domain then is their form the same as those derived from an inner product equality. In fact, if we try to maximize the integral of the energy over the whole domain (as opposed to the outlet energy only), a source term arises in the adjoint equations (Cathalifaud & Luchini 2000; Zuccher *et al.* 2004, 2006). Unlike the continuous version of the Lagrange multiplier approach, examples where this technique is applied directly to the discrete equations are less numerous (Luchini & Bottaro 1998, 2001; Luchini 2000; Cathalifaud & Luchini 2000; Zuccher *et al.* 2004, 2006).

The adjoint methodology for the calculation of optimal perturbations, and in particular its discrete implementation, was introduced by Farrell & Moore (1992) in the context of oceanic flows. The use of the discrete approach has several advantages, among which the necessity of an ‘ad hoc’ adjoint code is avoided and a foolproof test is available by comparing the results of the direct and adjoint calculations, which must match to machine accuracy for any step size and not only in the limit of step size tending to zero (Zuccher *et al.* 2006). This is due to the conservation of a quantity which depends on x only (Luchini & Bottaro 1998; Luchini 2000). For a thorough discussion on the issue of continuous versus discrete adjoints the reader is referred to Gunzburger (2000).

The numerical discretization of a general parabolic system of partial differential equations such as (2.3) can be recast as

$$\mathbf{C}_{n+1} \mathbf{f}_{n+1} = \mathbf{B}_n \mathbf{f}_n \quad (3.9)$$

where n denotes the n th grid point in the streamwise direction x , \mathbf{f} is the vector of unknowns (not with only 5 elements but with $5 \times N_y$, where N_y is the number of grid points in the wall-normal direction y) and matrices \mathbf{C} and \mathbf{B} depend on x (as does the basic flow) and account for the discretization in both x and y . The solution is found by marching forward in space from $n = 0$ (x_{in}), given the initial condition \mathbf{f}_0 , to $n = N - 1$. The boundary conditions at the wall and for $y \rightarrow \infty$ are already included in the matrices rows. The discrete objective function we aim to maximize is $\mathcal{J} = \mathbf{f}_N^T \mathbf{M}_N \mathbf{f}_N$, where \mathbf{M}_N is the discrete version of $\tilde{\mathbf{M}}_{\text{out}}$ as defined in (3.4) and accounts for the discretization of the integral in y .

The augmented functional \mathcal{L} , which contains the objective function $\mathcal{J} = E_{\text{out}}$, the constraints (3.9) and $E_{\text{in}} = E_0$, and the Lagrange multipliers, is written as

$$\mathcal{L}(\mathbf{f}_0, \dots, \mathbf{f}_N) = \mathbf{f}_N^T \mathbf{M}_N \mathbf{f}_N + \sum_{n=0}^{N-1} [\mathbf{p}_n^T (\mathbf{C}_{n+1} \mathbf{f}_{n+1} - \mathbf{B}_n \mathbf{f}_n)] + \lambda_0 [\mathbf{f}_0^T \mathbf{M}_0 \mathbf{f}_0 - E_0] \quad (3.10)$$

where \mathbf{p}_n is the vector of Lagrangian multipliers, which depends on the streamwise location n and \mathbf{M}_0 is the discrete version of $\tilde{\mathbf{M}}_{\text{in}}$ as defined in (3.7), in the same fashion as \mathbf{M}_N . Only the dependence on \mathbf{f}_n ($n = 0, \dots, N$) has been emphasized in \mathcal{L} because its derivative with respect to the Lagrangian multipliers (which is needed to impose $\delta \mathcal{L} = 0$) would lead to the constraints that are already known. The summation between 0 and $N - 1$ in (3.10) involving \mathbf{p}_n reflects the integral along x . The integration by parts (which would be performed in the continuous case) is here replaced by adding and subtracting $\mathbf{p}_{n+1}^T \mathbf{B}_{n+1} \mathbf{f}_{n+1}$ in the summation so that the terms can be rearranged as

$$\begin{aligned} & \sum_{n=0}^{N-1} [\mathbf{p}_n^T (\mathbf{C}_{n+1} \mathbf{f}_{n+1} - \mathbf{B}_n \mathbf{f}_n)] \\ &= \sum_{n=0}^{N-1} [\mathbf{p}_n^T \mathbf{C}_{n+1} \mathbf{f}_{n+1} - \mathbf{p}_{n+1}^T \mathbf{B}_{n+1} \mathbf{f}_{n+1}] + \sum_{n=0}^{N-1} [\mathbf{p}_{n+1}^T \mathbf{B}_{n+1} \mathbf{f}_{n+1} - \mathbf{p}_n^T \mathbf{B}_n \mathbf{f}_n] \\ &= \sum_{n=0}^{N-1} [\mathbf{p}_n^T \mathbf{C}_{n+1} \mathbf{f}_{n+1} - \mathbf{p}_{n+1}^T \mathbf{B}_{n+1} \mathbf{f}_{n+1}] + \mathbf{p}_N^T \mathbf{B}_N \mathbf{f}_N - \mathbf{p}_0^T \mathbf{B}_0 \mathbf{f}_0, \end{aligned}$$

and expression (3.10) can be rewritten as

$$\begin{aligned} \mathcal{L}(\mathbf{f}_0, \dots, \mathbf{f}_N) &= \mathbf{f}_N^T \mathbf{M}_N \mathbf{f}_N + \sum_{n=0}^{N-1} [\mathbf{p}_n^T \mathbf{C}_{n+1} \mathbf{f}_{n+1} - \mathbf{p}_{n+1}^T \mathbf{B}_{n+1} \mathbf{f}_{n+1}] \\ &\quad + \mathbf{p}_N^T \mathbf{B}_N \mathbf{f}_N - \mathbf{p}_0^T \mathbf{B}_0 \mathbf{f}_0 + \lambda_0 [\mathbf{f}_0^T \mathbf{M}_0 \mathbf{f}_0 - E_0]. \end{aligned} \quad (3.11)$$

As in the continuous case, the stationary condition is found when $\delta \mathcal{L} = 0$

$$\frac{\delta \mathcal{L}}{\delta \mathbf{f}_0} \delta \mathbf{f}_0 + \sum_{n=0}^{N-2} \left[\frac{\delta \mathcal{L}}{\delta \mathbf{f}_{n+1}} \delta \mathbf{f}_{n+1} \right] + \frac{\delta \mathcal{L}}{\delta \mathbf{f}_N} \delta \mathbf{f}_N = 0,$$

which, in order to be satisfied for any arbitrary \mathbf{f}_0 , \mathbf{f}_{n+1} and \mathbf{f}_N , leads to

$$\frac{\delta \mathcal{L}}{\delta \mathbf{f}_0} = -\mathbf{p}_0^T \mathbf{B}_0 + 2\lambda_0 \mathbf{f}_0^T \mathbf{M}_0 = 0, \quad (3.12)$$

$$\frac{\delta \mathcal{L}}{\delta \mathbf{f}_{n+1}} = \mathbf{p}_n^T \mathbf{C}_{n+1} - \mathbf{p}_{n+1}^T \mathbf{B}_{n+1} = 0, \quad n = 0, \dots, N-1, \quad (3.13)$$

$$\frac{\delta \mathcal{L}}{\delta \mathbf{f}_N} = 2 \mathbf{f}_N^T \mathbf{M}_N + \mathbf{p}_N^T \mathbf{B}_N = 0. \quad (3.14)$$

Equation (3.12) furnishes the optimality condition to be satisfied at x_{in} and equation (3.13) leads to

$$\mathbf{p}_n^T \mathbf{C}_{n+1} - \mathbf{p}_{n+1}^T \mathbf{B}_{n+1} = 0, \quad (3.15)$$

which is the discrete form of the adjoint equations to be solved by marching backwards from x_{out} to x_{in} with the initial condition provided by equation (3.14) solved for \mathbf{p}_N .

3.2.1. Outlet conditions

From expression (3.14) follows

$$\mathbf{B}_N^T \mathbf{p}_N = -2 \mathbf{M}_N^T \mathbf{f}_N \quad (3.16)$$

where \mathbf{B}_N is the discrete representation of $\mathbf{H}_{1\text{out}}$ and is singular because the fifth column in \mathbf{H}_1 is made up of zeros as $p_x = 0$ in this approximation (the last column of matrix \mathbf{A} is made up of zeros). This implies that the solution cannot be found unless the solvability condition is satisfied. The singularity of \mathbf{H}_1 is not simply a practical numerical problem for the solution of (3.16) but contains deeper information and insights regarding the initial condition for the adjoint variables. The impossibility of determining a unique solution of (3.16) translates into the fact that at least one out of five adjoint variables is free at $x = x_{\text{out}}$ and therefore can be chosen arbitrarily. For simplicity, we set p_5 (the fifth adjoint variable) to zero.

3.2.2. Inlet conditions

By imposing $\delta \mathcal{L} / \delta \mathbf{f}_{\text{in}} = 0$ condition (3.12) was obtained. The operator \mathbf{M}_0 is the discrete counterpart of \mathbf{M}_{in} and is singular (as \mathbf{M}_{out}) so \mathbf{M}_0^{-1} does not exist and (3.12) cannot be solved. However, \mathbf{M}_0 is diagonal and therefore the j th element of \mathbf{f}_0 corresponding to $\mathbf{M}_{0jj} \neq 0$ can be retrieved from

$$\mathbf{f}_{0j} = \begin{cases} \frac{(\mathbf{p}_0^T \mathbf{B}_0)_j}{2 \lambda_0 \mathbf{M}_{0jj}} & \text{if } \mathbf{M}_{0jj} \neq 0 \\ 0 & \text{if } \mathbf{M}_{0jj} = 0. \end{cases} \quad (3.17)$$

The multiplier λ_0 is found by imposing the constraint $E_0 = E_{\text{in}}$.

3.3. An optimization algorithm

The constrained optimization developed above has enabled us to write a set of equations and boundary conditions that must be satisfied simultaneously. More specifically, we first need to solve system (3.9) from $x = x_{\text{in}}$ ($n = 0$) to $x = x_{\text{out}}$ ($n = N - 1$) with initial conditions at x_{in} expressed by (3.17). We refer to this as the direct or forward problem. Then we need to solve system (3.15) from $x = x_{\text{out}}$ ($n = N - 1$) to $x = x_{\text{in}}$ ($n = 0$), with initial conditions derived from (3.16) and provided at $x = x_{\text{out}}$. We call this the adjoint or backward problem.

A quite large system of linear equations supplemented by initial and boundary conditions has to be solved. Instead of doing it in one step, however, we employ the intrinsic parabolic nature of the equations to efficiently solve separately the two coupled problems. Such an algorithm can be outlined in the following few steps:

1. a guessed initial condition $\mathbf{f}_{\text{in}}^{(0)}$ is provided at the beginning of the optimization procedure;

2. the forward problem (3.9) is solved at the i th iteration with the initial condition $f_{\text{in}}^{(i)}$;
3. the objective function $\mathcal{J}^{(i)} = E_{\text{out}}^{(i)}$ is computed at the end of the forward iteration and compared to the objective function $\mathcal{J}^{(i-1)} = E_{\text{out}}^{(i-1)}$ at the end of the previous forward iteration. If $|\mathcal{J}^{(i)}/\mathcal{J}^{(i-1)} - 1| < \epsilon_t$ (where ϵ_t is the maximum tolerance accepted to stop the optimization) then the optimization is considered converged;
4. if $|\mathcal{J}^{(i)}/\mathcal{J}^{(i-1)} - 1| > \epsilon_t$ the initial conditions for the backward problem (3.16) are assigned at the outlet and derived from the direct solution at $x = x_{\text{out}}$;
5. the backward problem (3.15) is solved from $x = x_{\text{out}}$ to $x = x_{\text{in}}$;
6. a new initial condition for the forward problem $f_{\text{in}}^{(i+1)}$ is obtained from the solution of the backward problem at $x = x_{\text{in}}$ employing (3.17);
7. the loop is repeated from step 2 on.

A similar iterative approach was first introduced by Farrell & Moore (1992) for obtaining the most rapidly growing perturbations in oceanic flows.

It should be noted that the above procedure does not necessarily guarantee convergence. If there is an attractor for the solution, then the procedure will capture it and this happens quite fast (2–3 forward–backward iterations) when the norm proposed by Luchini (2000) is used. On the other hand, it was observed that when the full energy norm is employed the convergence is generally much slower, depending on the wavenumber β , reaching the fastest convergence in the proximity of the optimal β .

4. Discretization

A finite difference discretization scheme has been implemented to numerically solve equations (2.3) with boundary conditions (2.2). For generality, grid points in x and y are not necessarily equally spaced. A staggered grid is introduced in the wall-normal direction, with variables u , v , w and T known at the grid points, and p known at the mid-grid (staggered) points. All equations are satisfied at the grid points except for continuity, which is satisfied at the mid-grid points. The use of the uneven grid in y allows us to cluster more nodes close to the wall so as to take into account the large gradients of boundary layer quantities in this region.

The last point of the y -grid is located far enough from the wall to allow us to specify there the boundary conditions for $y \rightarrow \infty$.

Fourth-order non-compact finite differences are used for the y discretization, employing six points so as to allow fourth-order accuracy for the second derivative. By using six points, the first derivative is automatically fifth-order accurate and the function (when interpolated due to the staggered grid) is sixth-order accurate.

Also, the discretization in the streamwise direction is based on an uneven grid. Since the system of boundary layer equations is parabolic, a second-order backward discretization is chosen, which requires the solution at two previous steps to be known. For the first step, however, a first-order scheme is used because only the initial condition is available.

After the discretization, the original system of partial differential equations (2.3) can be re-written in the following form:

$$[C_{n+1}^0 \mathbf{H}_{n+1}^1 + \mathbf{H}_{n+1}^2] \mathbf{f}_{n+1} = -C_{n+1}^1 \mathbf{H}_n^1 \mathbf{f}_n - C_{n+1}^2 \mathbf{H}_{n-1}^1 \mathbf{f}_{n-1} \quad (4.1)$$

where coefficients C_{n+1}^0 , C_{n+1}^1 and C_{n+1}^2 account for the streamwise discretization and matrices \mathbf{H}_{n+1}^1 and \mathbf{H}_{n+1}^2 are the discretized versions of respectively \mathbf{H}_1 and \mathbf{H}_2

introduced in §2. The solution is thus completely determined once the initial condition $\mathbf{f}_0 = \mathbf{f}_{\text{in}}$ is given at x_{in} .

Equation (4.1) can be easily rewritten in a form similar to (3.9),

$$\mathbf{C}_{n+1} \mathbf{f}_{n+1} = C_{n+1}^1 \mathbf{B}_n \mathbf{f}_n + C_{n+1}^2 \mathbf{B}_{n-1} \mathbf{f}_{n-1}, \quad (4.2)$$

where $\mathbf{C}_{n+1} = [C_{n+1}^0 \mathbf{H}_{n+1}^1 + \mathbf{H}_{n+1}^2]$ and $\mathbf{B}_n = -\mathbf{H}_n^1$.

Unlike the simple form (3.9), which refers to a scheme where the new solution \mathbf{f}_{n+1} depends on \mathbf{f}_n only, the discrete equation (4.1) depends on \mathbf{f}_n and \mathbf{f}_{n-1} due to the second-order approximation in x . Therefore, the discrete adjoint system is slightly different from (3.15). More specifically, by repeating the same steps as in §3.2, the constraint $\mathbf{C}_{n+1} \mathbf{f}_{n+1} - C_{n+1}^1 \mathbf{B}_n \mathbf{f}_n - C_{n+1}^2 \mathbf{B}_{n-1} \mathbf{f}_{n-1} = 0$ is left-multiplied by the vector of Lagrangian multipliers \mathbf{p}_n and then all terms are included in the summation on n (in the streamwise direction) to form the functional for the constrained optimization. Within this summation, we first add and subtract the quantity $\mathbf{p}_{n+1}^\top [C_{n+2}^1 \mathbf{B}_{n+1} \mathbf{f}_{n+1} + C_{n+2}^2 \mathbf{B}_n \mathbf{f}_n]$ and rearrange the summation as $\sum \mathbf{p}_n^\top [\mathbf{C}_{n+1} \mathbf{f}_{n+1}] - \sum \mathbf{p}_{n+1}^\top [C_{n+2}^1 \mathbf{B}_{n+1} \mathbf{f}_{n+1} + C_{n+2}^2 \mathbf{B}_n \mathbf{f}_n]$ and then we add and subtract the quantity $\mathbf{p}_{n+2}^\top [C_{n+3}^1 \mathbf{B}_{n+1} \mathbf{f}_{n+1}]$ so that the final form of the summation is $\sum \mathbf{p}_n^\top [\mathbf{C}_{n+1} \mathbf{f}_{n+1}] - \sum \mathbf{p}_{n+1}^\top [C_{n+2}^1 \mathbf{B}_{n+1} \mathbf{f}_{n+1}] - \sum \mathbf{p}_{n+2}^\top [C_{n+3}^2 \mathbf{B}_{n+1} \mathbf{f}_{n+1}]$. In this way, all terms are right-multiplied by \mathbf{f}_{n+1} so that the derivative of the functional \mathcal{L} with respect to \mathbf{f}_{n+1} leads to the adjoint discrete equation in the form

$$\mathbf{p}_n^\top \mathbf{C}_{n+1} - \mathbf{p}_{n+1}^\top C_{n+2}^1 \mathbf{B}_{n+1} - \mathbf{p}_{n+2}^\top C_{n+3}^2 \mathbf{B}_{n+1} = 0, \quad (4.3)$$

where the solution at step n is obtained by marching upstream in space from the outlet to the inlet and needs two steps downstream to be computed.

5. The basic-flow model

The basic flow for the flat plate is the same as in Tumin & Reshotko (2003) and is obtained from a conventional similarity solution.

For the high-speed flow past a sphere, the streamwise velocity U_e at the edge of the boundary layer of the subsonic part of the flow can be approximated by

$$U_e = \left. \frac{dU_e}{d\theta} \right|_0 \theta,$$

where $dU_e/d\theta|_0$ is the derivative of the edge velocity with respect to the meridional coordinate θ evaluated at the stagnation point. This quantity can be calculated from the modified Newtonian pressure distribution (Anderson 2000) as

$$\frac{1}{U_\infty} \left. \frac{dU_e}{d\theta} \right|_0 = \sqrt{\frac{C_{p_{\text{max}}} \rho_\infty}{\rho_0}}$$

with $C_{p_{\text{max}}}$ (maximum pressure coefficient) and ρ_0 evaluated at the stagnation point for a calorically perfect gas with specific heat ratio $\gamma = 1.4$. Flow parameters at the edge of the boundary layer for the downstream locations can then be found from the isentropic relationships.

For the compressible boundary layer we consider the local-similarity approximation (Anderson 2000) and introduce the Levy–Lees–Dorodnitsyn variables

$$\xi = \int_0^\theta \rho_e \mu_e U_e R^3 (\sin \theta)^2 d\theta, \quad \bar{\eta} = \frac{\rho_e U_e R \sin \theta}{\sqrt{2\xi}} \int_0^\eta \frac{\rho}{\rho_e} d\eta,$$

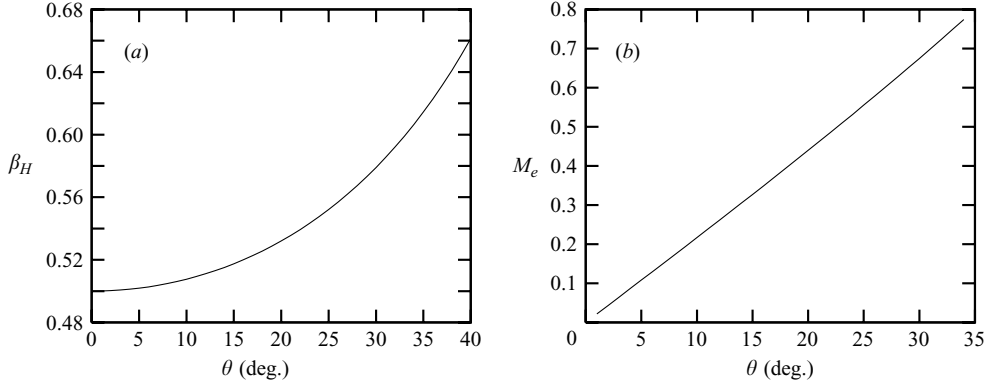


FIGURE 1. (a) Hartree parameter β_H and (b) local Mach number M_e at the edge of the boundary layer, as a function of the meridional angle θ .

where $\eta = y/H_{\text{ref}}$, y being the coordinate in the wall-normal direction. After substituting these new variables ξ and $\bar{\eta}$, boundary-layer equations can be recast as

$$(Cf'')' + ff'' + \beta_H \left[\frac{\rho}{\rho_e} - (f')^2 \right] = 0,$$

$$\left(\frac{C}{Pr} \hat{g}' \right)' + f \hat{g}' + \frac{(\gamma - 1)M_e^2}{1 + \frac{1}{2}(\gamma - 1)M_e^2} \left[C \left(1 - \frac{1}{Pr} \right) ff'' \right]' = 0,$$

where the prime denotes the partial derivative with respect to $\bar{\eta}$, $C = (\rho\mu)/(\rho_e\mu_e)$ and $\beta_H = (2\xi/U_e)dU_e/d\xi$ is the Hartree parameter. These boundary layer equations are solved subject to the conventional boundary layer conditions on the wall and in the free stream (Anderson 2000). The flow quantities are then retrieved from functions $f(\xi, \bar{\eta})$ and $\hat{g}(\xi, \bar{\eta})$, which are related to the velocity $U(\xi, \bar{\eta})$ and total enthalpy $I(\xi, \bar{\eta})$ according to the similarity laws

$$U(\xi, \bar{\eta}) = U_e(\xi)f'(\xi, \bar{\eta}), \quad I(\xi, \bar{\eta}) = I_e\hat{g}(\xi, \bar{\eta}).$$

As proved in figures 1(a) and 1(b), for $\theta \leq 30^\circ$ β_H lies within the interval $[0.5; 0.6]$ and the Mach number is a linear function of θ . Moreover, when the wall-normal distance is scaled with $H(\theta) = \sqrt{2\xi}/(\rho_e U_e R \sin \theta)$ profiles of U/U_e and T/T_e are almost independent of the Mach number M_e and Hartree parameter β_H , as shown in figures 2(a) and 2(b).

The dependence on the meridional angle θ enters the analysis only through the local velocity, temperature, density and pressure at the edge of the boundary layer, and through the local length scale $H(\theta)$, which is however a slow function of θ as figure 3 clearly shows.

For the present study we have chosen the scaled velocity and temperature profiles obtained for $M_e = 0.6$ and $\beta_H = 0.5$.

6. Results

Results for the flat plate and sphere are discussed here. In the first case the code was verified against incompressible (Andersson *et al.* 1999) and compressible (Tumin & Reshotko 2003) published works, in which spectral collocation methods (SCM) were employed.

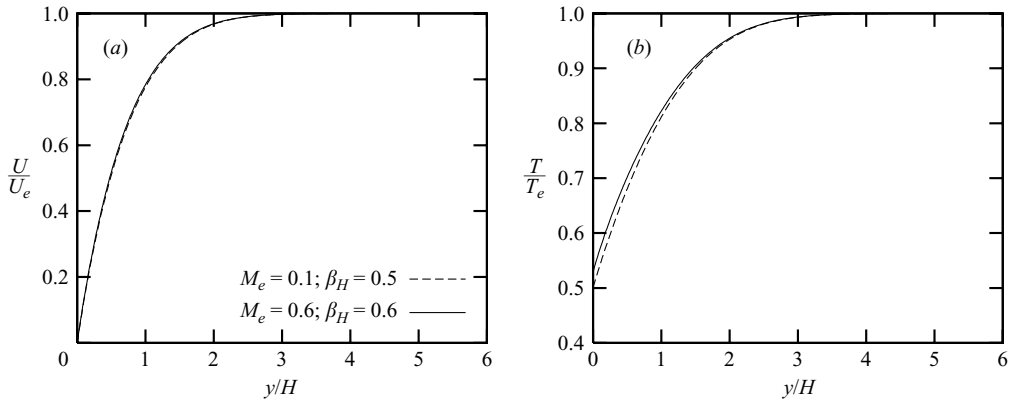


FIGURE 2. Effect of the Mach number M_e and Hartree parameter β_H on the basic flow profiles: (a) streamwise velocity, (b) temperature.

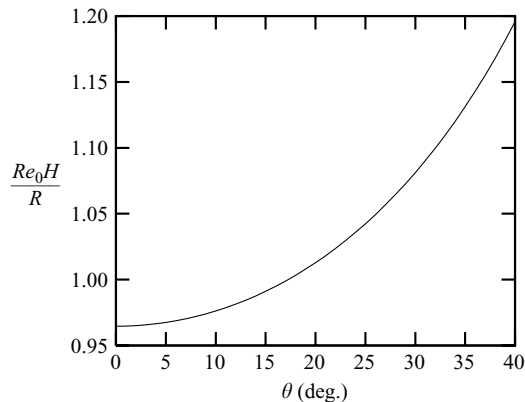


FIGURE 3. Boundary layer local length scale $Re_0 H/R$ as a function of the meridional angle θ .
 $Re_0 = \sqrt{\rho_0} U_\infty R / \mu_0$.

In figure 4 the gain $G\epsilon^2 = G/Re$, where $G = E_{\text{out}}/E_{\text{in}}$, is shown in the limit $Re \rightarrow \infty$ as a function of the wavenumber β for the incompressible flow past a flat plate and compared with previous results available in the literature. The agreement is very good, though present values of the gain are very slightly smaller than those obtained by Andersson *et al.* (1999). This might be due to the different numerical implementations.

In what follows, for the flat-plate case, only results regarding the use of the full energy norm at the outlet (FENO), i.e. norm (3.2), are considered and compared to those obtained by Tumin & Reshotko (2003), in which partial energy norm at the outlet (PENO) was employed (i.e. only u_{out} and T_{out} were non-zero, whereas v_{out} and w_{out} were excluded from (3.2)). In both cases the inlet energy norm is the one introduced by Luchini (2000) and extended to the compressible case as in (3.5). We refer to (3.5) as partial energy norm at the inlet (PENI), as it considers the contributions of v_{in} and w_{in} only. The choice of this inlet norm is further discussed in § 7.

For the sphere case, the code for optimal perturbations was verified against Tumin & Reshotko (2004) (SCM) and results are presented later for both partial (PENO) and full (FENO) energy norm at the outlet, keeping the inlet norm fixed (PENI).

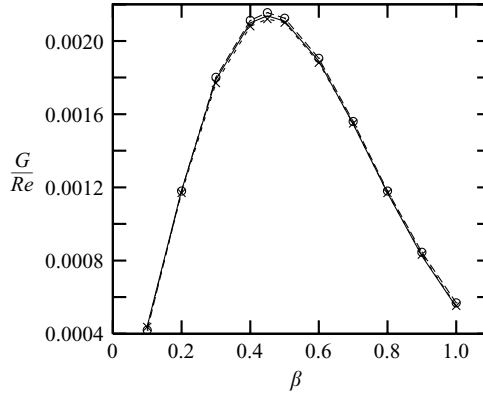


FIGURE 4. Comparison of G/Re as a function of the wavenumber β with previous results available in literature for the incompressible case in the limit $Re \rightarrow \infty$. Solid line, present; \circ , Andersson *et al.* (1999); \times , Tumin & Reshotko (2003). $M = 0.02$, $x_{in} = 0$, $x_{out} = 1.0$, $T_w/T_{ad} = 1$.

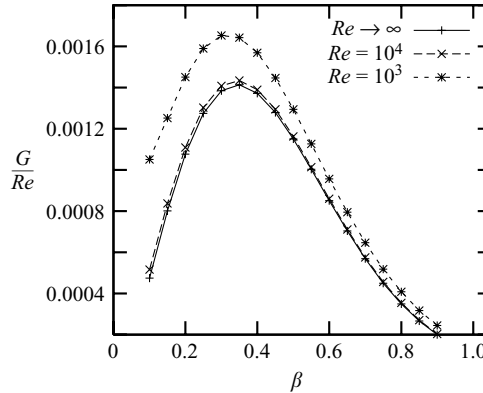


FIGURE 5. Objective function $\mathcal{J} = G/Re$: effect of Re and β for $M = 3$, $T_w/T_{ad} = 0.5$, $x_{in} = 0$, $x_{out} = 1.0$.

6.1. Flat plate

Here we consider a perfect gas with a specific heat ratio $\gamma = 1.4$, Prandtl number $Pr = 0.7$ and viscosity depending on T only, in accordance with the Sutherland law. The stagnation temperature T_0 is fixed and equal to 333 K.

As described in §3.1, the full energy norm at the outlet (FENO) includes not only u and T (as in Tumin & Reshotko (2003)) but also also v and w . At the inlet, PENI includes only v and w .

Figure 5 shows the effect of the Reynolds number Re on G/Re when PENI and FENO are employed. The plot refers to the case with Mach number $M = 3$, $T_w/T_{ad} = 0.5$ (T_w is the wall temperature and T_{ad} is the recovery temperature), initial station for the computation $x_{in} = 0$, and outlet station $x_{out} = 1.0$. It is clear that the Reynolds number has quite a strong influence only for $Re < 10^4$, while for values greater than this limit, results do not differ significantly from the Reynolds-number-independent case.

The effect of the norm (PENI versus FENO) for different temperature factors T_w/T_{ad} at $M = 0.5$ is reported in figure 6(a) ($x_{in} = 0$, $x_{out} = 1.0$). The Reynolds

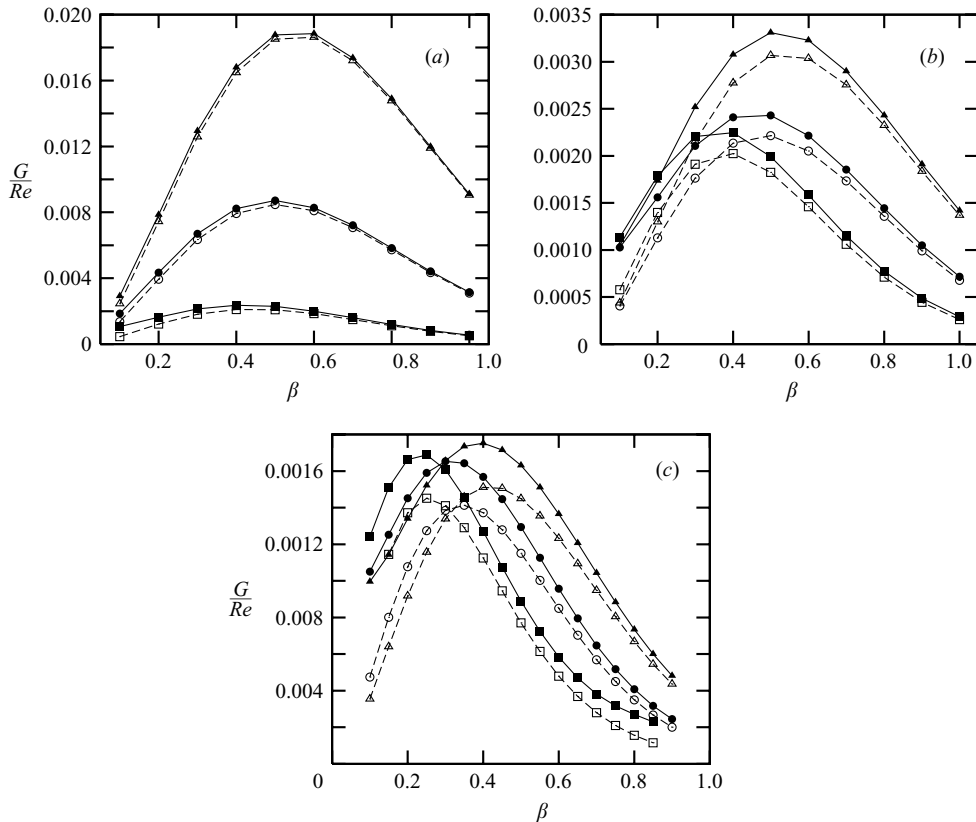


FIGURE 6. Objective function $\mathcal{J} = G/Re$: effect of β , T_w/T_{ad} and norm choice PENO (only u^2 and T^2 at x_{out}) versus FENO. PENO at the inlet (only v^2 and w^2 at x_{in}), $Re = 10^3$, $x_{in} = 0$ $x_{out} = 1.0$. \square , $T_w/T_{ad} = 1.00$; \circ , $T_w/T_{ad} = 0.50$; \triangle , $T_w/T_{ad} = 0.25$; full symbols and solid lines refer to FENO, empty symbols and dashed lines to PENO. (a) $M = 0.5$, (b) $M = 1.5$, (c) $M = 3.0$.

number for the case of full energy norm at the outlet (FENO) is $Re = 10^3$. It can be concluded that at low Mach number $M = 0.5$, though large enough to allow compressible effects, the choice of the norm does not produce a significant difference.

The conclusion drawn from figure 6(a) does not extend to larger values of Mach number. In figure 6(b), a moderate supersonic Mach number $M = 1.5$ is considered. The effect of increasing M is clearly to shift the maximum of the curves towards smaller values of β and to enhance the difference between results obtained with different norms. This is particularly true for $T_w/T_{ad} = 1.00$.

In the supersonic case, $M = 3$, reported in figure 6(c), a difference up to 17% can be detected when comparing PENO with FENO. This difference is significantly higher for low values of the wavenumber β and is visible also in figure 2 of Andersson *et al.* (1999) for $M = 0$.

It can thus be concluded that for the flat-plate case results obtained with an energy norm including u , v , w and T at the outlet (FENO) are significantly different from those where only u and T are considered and that this effect increases with the Mach number.

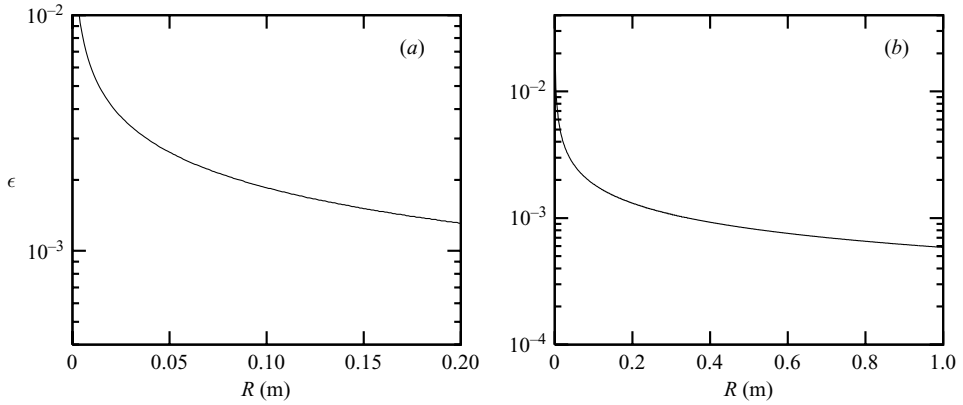


FIGURE 7. Estimate parameter ϵ at: (a) wind tunnel conditions: $M = 6$, $p_0 = 25$ bar, $T_0 = 750$ K; (b) flight conditions: $M_\infty = 6$, $p_\infty = 0.0253$, bar, $T_\infty = 217$ K; $\theta_{ref} = 30.0^\circ$ for both cases.

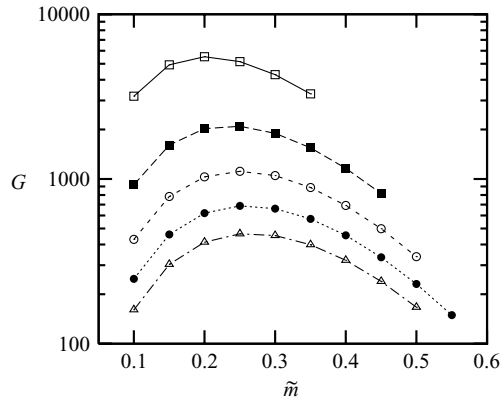


FIGURE 8. Objective function $\mathcal{J} = G$: effect of ϵ and $\tilde{m} = m\epsilon$ for $\theta_{in} = 10.0^\circ$, $\theta_{out} = 15.0^\circ$, $\theta_{ref} = 30.0^\circ$, $T_w/T_{ad} = 0.5$. Partial energy norm at both inlet and outlet (PENI and PENO). \square , $\epsilon = 2.5 \times 10^{-4}$; \blacksquare , $\epsilon = 5.0 \times 10^{-4}$; \circ , $\epsilon = 7.5 \times 10^{-4}$; \bullet , $\epsilon = 1.0 \times 10^{-3}$; \triangle , $\epsilon = 1.25 \times 10^{-3}$.

6.2. Sphere

In the case of the sphere, the solution of the governing equations is assumed to be proportional to $\exp(im\phi)$, where m is the azimuthal index and i the imaginary unit (see the Appendix).

In order to estimate the values of the small parameter ϵ that might be of interest to the analysis, we consider two examples at a free-stream Mach number $M_\infty = 6$. The first one corresponds to typical wind tunnel conditions, $T_0 = 750$ K and $p_0 = 25$ bar. The second case is chosen as a flight condition, with $T_\infty = 217$ K and $p_\infty = 0.0253$ bar. Figure 7 illustrates typical values of ϵ as a function of the sphere radius R (in metres) and evaluated at the reference parameters corresponding to the edge of the boundary layer at $\theta_{ref} = 30^\circ$. One can see that values of ϵ on the order or 10^{-3} correspond to realistic cases.

In what follows, the edge boundary layer parameters are defined at $\theta_{ref} = 30^\circ$. This choice has an impact on the definition of ϵ , but the final result $G\epsilon^2 = E_{out}/E_{in}$ is independent of the reference point θ_{ref} .

The effect of ϵ on the gain G as a function of \tilde{m} ($\tilde{m} = m\epsilon$) is shown in figure 8, where the partial energy norm is used at both inlet and outlet (PENI and PENO). Unlike

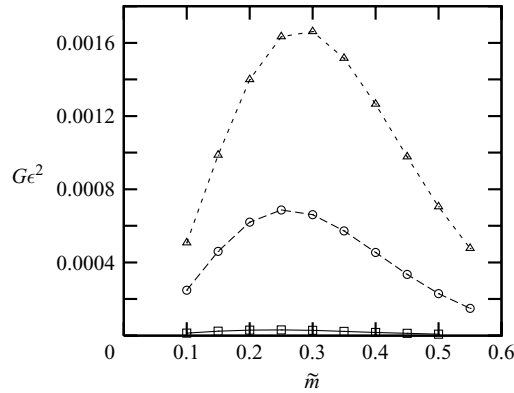


FIGURE 9. Objective function $\mathcal{J} = G\epsilon^2$: effect of wall temperature ratio T_w/T_{ad} and $\tilde{m} = m\epsilon$ for $\theta_{in} = 10.0^\circ$, $\theta_{out} = 15.0^\circ$, $\theta_{ref} = 30.0^\circ$, $\epsilon = 10^{-3}$. Partial energy norm at both inlet and outlet (PENI and PENO). \square , $T_w/T_{ad} = 1.00$; \circ , $T_w/T_{ad} = 0.50$; \triangle , $T_w/T_{ad} = 0.25$.

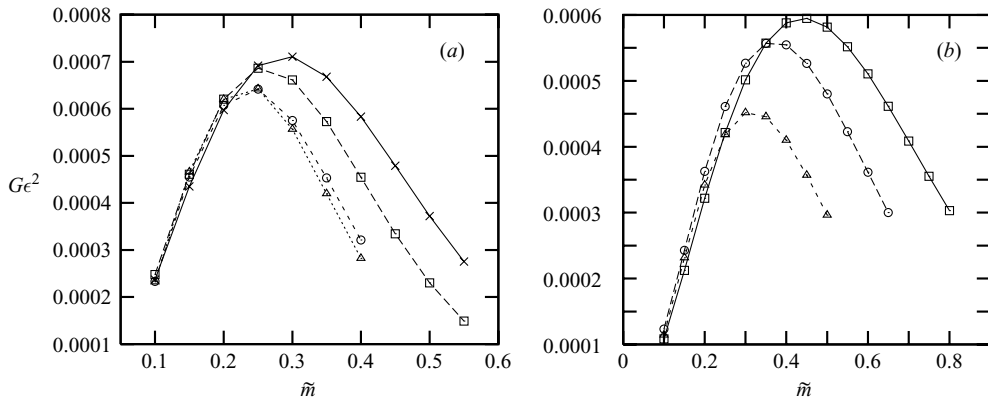


FIGURE 10. Objective function $\mathcal{J} = G\epsilon^2$: effect of outlet station θ_{out} and $\tilde{m} = m\epsilon$ for $\theta_{ref} = 30.0^\circ$, $T_w/T_{ad} = 0.5$, $\epsilon = 10^{-3}$. Partial energy norm at both inlet and outlet (PENI and PENO). (a) $\theta_{in} = 10.0^\circ$: \times , $\theta_{out} = 13^\circ$; \square , $\theta_{out} = 15^\circ$; \circ , $\theta_{out} = 20^\circ$; \triangle , $\theta_{out} = 25^\circ$. (b) $\theta_{in} = 15.0^\circ$: \square , $\theta_{out} = 18^\circ$; \circ , $\theta_{out} = 20^\circ$; \triangle , $\theta_{out} = 25^\circ$.

the parallel-flow formulation (Reshotko & Tumin 2004) where the Reynolds number and the curvature radius are independent, here the radius is strictly associated with the Reynolds number and not only with the curvature. Assuming that all reference parameters are constant, when the radius increases ϵ decreases ($\epsilon = \sqrt{\nu_{ref}/RU_{ref}}$) leading to an increase of the gain, as reported in figure 8.

The effect of wall temperature T_w/T_{ad} is illustrated in figure 9. Similarly to previous studies (Reshotko & Tumin 2000; Tumin & Reshotko 2001, 2003), the cooling of the wall destabilizes the flow with respect to the transient energy growth and the difference in G with respect to the adiabatic wall is about two orders of magnitude.

Figure 10(a) shows the effect of the outlet station θ_{out} and \tilde{m} for $\theta_{in} = 10.0^\circ$, $\theta_{ref} = 30.0^\circ$, $T_w/T_{ad} = 0.5$ and $\epsilon = 10^{-3}$. It is clear that the maximum transient growth is achieved for smallest intervals of the θ range, more specifically for $\theta \in [10^\circ; 13^\circ]$.

The trend observed in figure 10(a) can be found also in figure 10(b), where the same kind of plot is reported, but for $\theta_{in} = 15.0^\circ$ instead of $\theta_{in} = 10.0^\circ$. Again, the smallest range of meridional angles produces the largest energy growth.

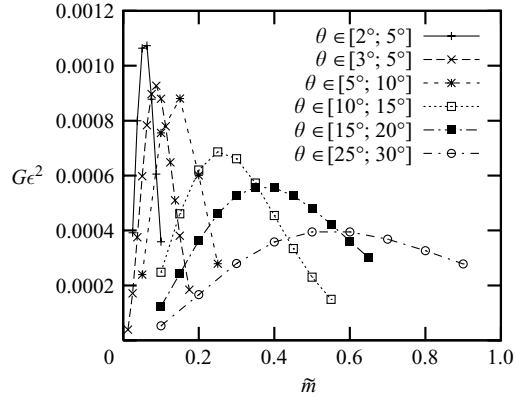


FIGURE 11. Objective function $\mathcal{J} = G\epsilon^2$: effect of interval location and $\tilde{m} = m\epsilon$ for $\theta_{\text{ref}} = 30.0^\circ$, $T_w/T_{\text{ad}} = 0.5$, $\epsilon = 10^{-3}$. Partial energy norm at both inlet and outlet (PENI and PENO).

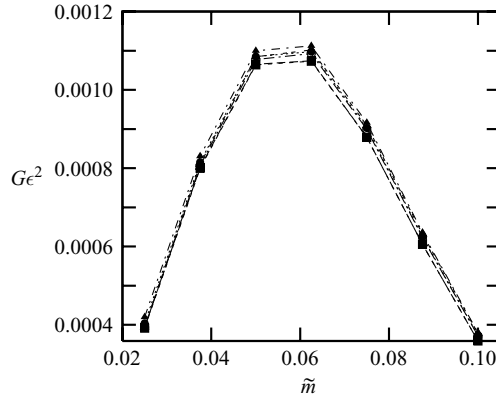


FIGURE 12. Objective function $\mathcal{J} = G\epsilon^2$: effect of ϵ , choice of the energy norm (FENO versus PENO, for PENI) and $\tilde{m} = m\epsilon$ for $\theta_{\text{in}} = 2.0^\circ$, $\theta_{\text{out}} = 5.0^\circ$, $\theta_{\text{ref}} = 30.0^\circ$, $T_w/T_{\text{ad}} = 0.5$. \square , $\epsilon = 1 \times 10^{-3}$; \circ , $\epsilon = 2 \times 10^{-3}$; \triangle , $\epsilon = 3 \times 10^{-3}$; full symbols refer to FENO, empty ones to PENO.

Figure 11 provides better insight into the dependence of G on the choice of θ_{in} and θ_{out} . The difference $\theta_{\text{out}} - \theta_{\text{in}}$ is not the only factor that causes a larger energy growth. In fact, curves with the same $\theta_{\text{out}} - \theta_{\text{in}}$ (5°) but with different θ_{in} clearly show that the strongest transient growth is achieved close to the stagnation point.

The main outcome from the results presented up to this point and referred to the partial energy norm at both inlet and outlet (PENI and PENO) is a large transient energy growth in the proximity of the stagnation point. Moreover, this effect is much stronger when the difference $\theta_{\text{out}} - \theta_{\text{in}}$ is small. Due to the short downstream development of the flow, it is possible that the optimal perturbation in the form of counter-rotating vortices still dominates the flow field and therefore the choice of the partial energy norm at the outlet could be misleading. The use of the full energy norm (which encompasses not only u and T but also v and w) at the outlet would clarify this issue.

Figure 12 shows the effect of norm choice and ϵ . Quite a number of curves are reported because comparisons of FENO have meaning depending on the value of ϵ ,

but results with the PENO change with ϵ as well. In all cases the inlet energy norm is fixed (PENI). The constant parameters are $\theta_{\text{in}} = 2.0^\circ$, $\theta_{\text{out}} = 5.0^\circ$, $\theta_{\text{ref}} = 30.0^\circ$ and $T_w/T_{\text{ad}} = 0.5$. For $\epsilon = 10^{-3}$ there is basically no difference between using PENO and FENO. However, it is precisely in this range of ϵ that it is meaningful to investigate the behaviour of the solution, since it corresponds to the estimated values for wind tunnel conditions and flight tests, as reported in figure 7. For higher values of ϵ (2×10^{-3} and 3×10^{-3}) the difference between the use of the two norms seems to be more evident.

The conclusion from figure 12 is, however, that the maximum appreciable difference is confined to within about 1 % of the parameters of interest.

7. Shortcomings of the iterative algorithm

As mentioned before, the choice of the norm is not unique. Here we discuss some limitations of the iterative algorithm due to the choice of the inlet norm and focus on the incompressible case, for which previously published results obtained with different norms are available.

Andersson *et al.* (1999) employed the full norm including all components of velocity. By combining the continuity equation with the streamwise momentum equation (for the perturbations) and the continuity equation for the basic flow they derived a constraint that holds for each $x > 0$,

$$(\beta^2 - V_y)u + Vu_y - u_{yy} + U_yv - Uv_y - \beta U w = 0, \quad (7.1)$$

but optimal disturbances were computed at the leading edge of the flat plate, $x_{\text{in}} = 0$. In order to avoid discontinuity of the solution at $x = 0$, Andersson *et al.* (1999) required the optimal perturbation $[u_{\text{in}}, v_{\text{in}}, w_{\text{in}}]$ to satisfy the constraint (7.1) also at $x = 0^-$. However, since u , v and w at $x = 0^-$, as resulting from the application of the inlet conditions stemming from the adjoint-based iterative algorithm, do not satisfy (7.1), Andersson *et al.* (1999) needed to solve a further least-square problem seeking $[u_{\text{in}}, v_{\text{in}}, w_{\text{in}}]$ that simultaneously satisfy (7.1) and minimize the distance from the solution obtained by applying the inlet conditions (3.17).

It should be noticed that in Luchini (2000), where u_{in} was set to zero, no further constraints such as (7.1) were required because in that case v and w as resulting from the inlet conditions already satisfy the governing equations at $x_{\text{in}} = 0$, and there is no discontinuity in the solution.

From the point of view of optimization, what was done by Andersson *et al.* (1999) corresponds to adding more constraints to the problem. Because of this, the optimization procedure locates a maximum with a value of the objective function lower than in the case where the optimal perturbation is not constrained by an equation at the inlet.

Here we propose a further analysis of this issue.

By writing explicitly the inlet conditions (3.17), it is easy to verify that v_{in} and w_{in} go to zero at the wall as long as the streamwise component of the basic flow does, because they originate from the adjoint solution multiplied by U . Therefore, even if the adjoint field is not homogeneous at the wall, since U satisfies the no-slip condition, v_{in} and w_{in} are zero at the wall. On the other hand, the expression for u_{in} does not guarantee $u = 0$ at the wall and thus a non-homogeneous solution is allowed at the wall by the algorithm. However, this non-physical solution guarantees the maximum gain in the optimization procedure.

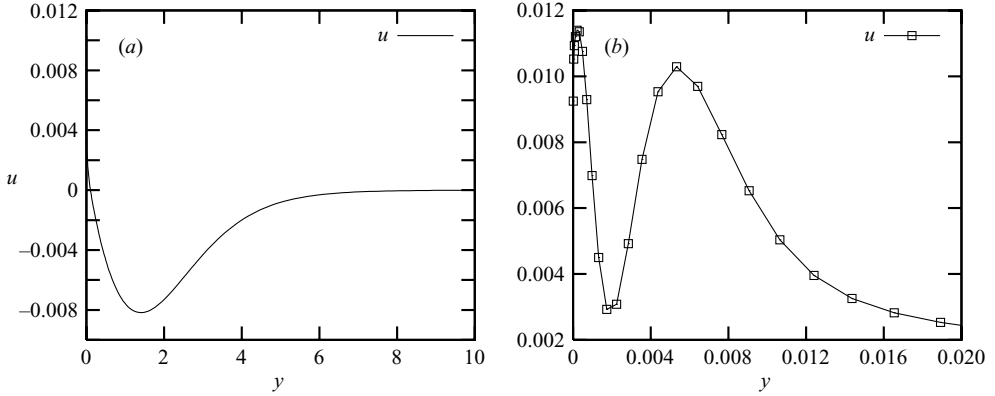


FIGURE 13. Profile of u_{in} as a function of y , no constraints on the initial condition, full energy norm at both inlet and outlet, $Re = 1000$. $M = 0.02$, $x_{in} = 0$ $x_{out} = 1.0$, $T_w/T_{ad} = 1$, $\beta = 0.55$. (a) Outer view. (b) Zoom in the proximity of the wall.

We consider adiabatic wall conditions, $T_w/T_{ad} = 1$, and free-stream Mach number $M = 0.02$. Figure 13 shows the streamwise component of the optimal perturbation obtained without any further constraint and using the full energy norm at both input and output (FENI and FENO). The outer view, figure 13(a), indicates that u_{in} does not satisfy the no-slip condition at the wall. Zooming in on the proximity of $y = 0$, figure 13(b), the behaviour of u_{in} is clearer, showing a few oscillations. These do not originate from the numerical scheme, as was proven by changing from fourth-order to second-order finite differences in y . On the contrary, they originate from the fact that u_{in} is generated by a component of the adjoint solution that does not guarantee $u_{in} = 0$ at the wall.

Different possible choices are available to render u_{in} homogeneous at the wall so as to reconcile the optimization algorithm with the governing equations. Such a ‘smoothing’, i.e. forcing $u_{in} = 0$ at the wall, avoids the discontinuity at $x_{in} = 0$ that would occur due to the fact that at $x = 0^+$ it must be $u = 0$ on the wall because of the no-slip condition.

The simplest approach is to substitute v_{in} and w_{in} as provided by the inlet conditions (3.17) into (7.1) and to obtain u_{in} from a boundary value problem where u_{in} is forced to be zero at the wall and in the free stream. By doing so, results reported in figure 14 are obtained. The order of magnitude of u is now much smaller than in figure 13, while v_{in} and w_{in} remain of the same order as before. This choice of rendering u_{in} zero at the wall so as to avoid the discontinuity at x_{in} , therefore, leads to an initial perturbation very far from the one originally computed without additional constraints and consequently generates a much lower gain.

If the goal is to try to keep u_{in} of the same order of magnitude as the profile originating from the inlet conditions alone (that in figure 13) but ensuring the continuity at x_{in} by imposing the $u_{in} = 0$ on the wall, then infinite possibilities are available.

We chose to replace the oscillations in u_{in} visible in figure 13 with a smooth solution so as to keep u_{in} unchanged from a certain \hat{y} to y_{max} (where the boundary conditions for $y \rightarrow \infty$ are imposed) and to replace u_{in} with a smooth function that goes to zero with y for $y < \hat{y}$. Both \hat{y} and the smooth function are arbitrary. For the function we need a choice that guarantees the continuity of u_{in} and its first and second derivative in \hat{y} (to avoid discontinuities when u_{in} is substituted in (7.1)) and such that its second

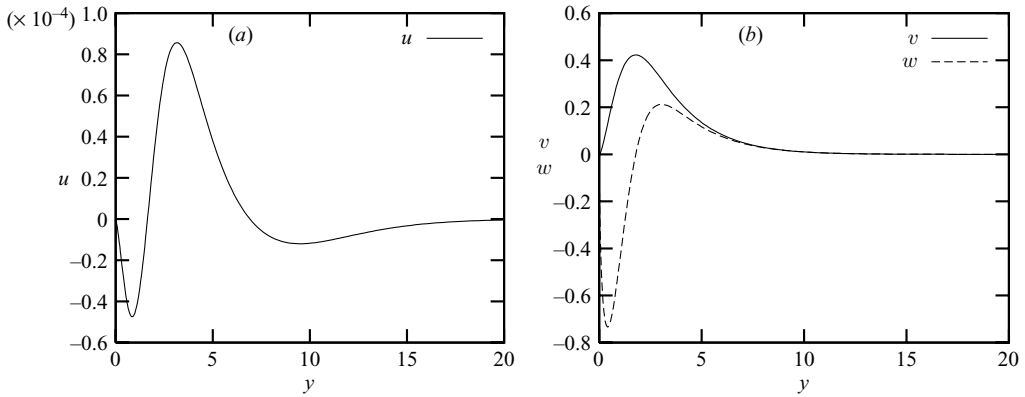


FIGURE 14. Profile of u_{in} , v_{in} and w_{in} as a function of y , physical, constrained solution. $M = 0.02$, $x_{in} = 0$, $x_{out} = 1.0$, $T_w/T_{ad} = 1$, $\beta = 0.55$. The constraint (7.1) is used where v_{in} and w_{in} are those originating from the inlet conditions (3.17) and u_{in} is calculated from the linear ordinary differential equation obtained by imposing homogeneous boundary conditions at the wall and in the free stream. (a) u_{in} , (b) v_{in} and w_{in} .

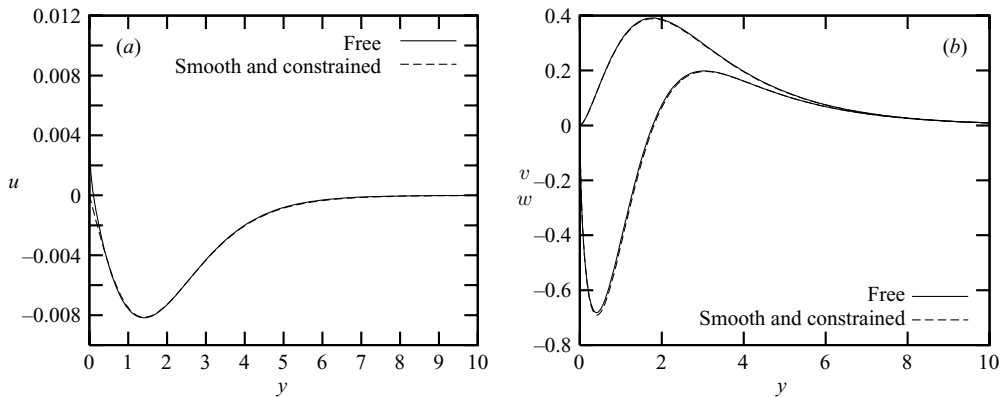


FIGURE 15. Profile of u_{in} , v_{in} and w_{in} as a function of y . Comparison between the ‘free’ solution computed from the inlet conditions (3.17) and the physical solution obtained by smoothing u_{in} and constraining it to be zero at the wall. The constraint (7.1) is used to compute w_{in} given u_{in} and v_{in} . $M = 0.02$, $x_{in} = 0$, $x_{out} = 1.0$, $T_w/T_{ad} = 1$, $\beta = 0.55$. (a) u_{in} , (b) v_{in} and w_{in} .

derivative is zero at the wall. The latter requirement is dictated by the constraint equation (7.1), from which it is easy to verify that at the wall $w = u_{yy}$. A fourth-order polynomial is used. The value of \hat{y} is chosen to be 80 % of the position in y where v_{in} reaches its maximum. After u_{in} has been smoothed, the constraint (7.1) is used to compute w_{in} given u_{in} and v_{in} .

This choice of smoothing u_{in} and constraining it to be zero at the wall produces a small difference (in the profile of u_{in}) with respect to the free case reported in figure 13 (see figure 15a), with the discrepancy localized in the proximity of the wall. On the other hand, no significant differences are detectable in the profiles of v_{in} and w_{in} (figure 15b). Since the optimal perturbation remains almost unchanged, the difference in the gain between the ‘free’ and ‘smooth and physical’ cases is very tiny. For the smoothed case the gain is $G/Re = 2.52 \times 10^{-3}$ as opposed to $G/Re = 2.54 \times 10^{-3}$ in the free case. This difference is about 0.8 %, even smaller than the tolerance

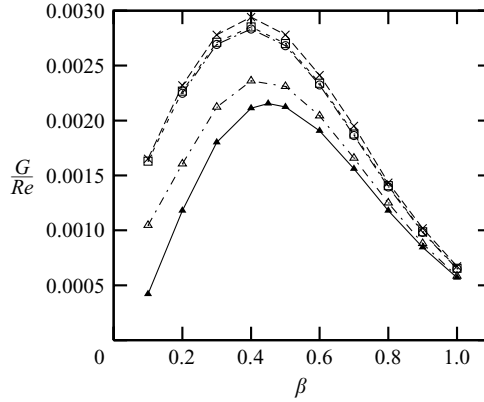


FIGURE 16. Comparison of G/Re between results obtained by Andersson *et al.* (1999) and present work. \times , Andersson *et al.* (1999), $Re = 1000$; \square , free optimization, $Re = 1000$; \circ , smooth and constrained, $Re = 1000$; \triangle , $u = 0$, $Re = 1000$; \blacktriangle , $Re \rightarrow \infty$. $M = 0.02$, $x_{in} = 0$, $x_{out} = 1.0$, $T_w/T_{ad} = 1$. Values of the gain are bounded between the free optimization results (upper limit – \square) and the Reynolds-number-independent ones (lower limit – \blacktriangle). Any constraint on the initial perturbation produces an energy gain that is within these limits.

(1%) which is required to end the forward–backward iteration in the optimization procedure presented in § 3.3.

Such a result offers much better insight into the issue of the inlet norm. It shows that in the constrained case the gain is, as expected, smaller than in the free case but this difference is extremely tiny and within the tolerance of the scheme. The explanation resides in the order of magnitude of u_{in} . If it is kept of the same order as resulting from the application of the automatic inlet conditions (3.17) then the gain is practically the same as in the case of unconstrained u_{in} . On the other hand, when u_{in} is obtained by solving the ordinary differential equation (7.1) assuming v_{in} and w_{in} given, a much smaller u_{in} is obtained with a considerable difference in the gain.

A summary of the above discussion is shown in figure 16, where different curves are reported. Results by Andersson *et al.* (1999) (\times) were obtained with the full energy norm at both inlet and outlet and show the largest values of the gain. They differ only slightly from those obtained in the present work for the case of free optimization (\square) and for the case of smoothed and constrained inflow profile (\circ). The maximum discrepancy is of the order of 3% and it is believed to be due to different numerical schemes, as the same trend was observed in the case of infinite Reynolds number (figure 4). Although it is not clear how the problem of discontinuity in u_{in} at the wall for $x_{in} = 0$ was treated by Andersson *et al.* (1999), our results illustrate that the energy gains are very close for constrained (smoothed u) and free optimizations.

Instead of employing a constraint equation, one can simply impose $u = 0$ at x_{in} (symbols \triangle in figure 16). This is one of the possible constraints that the optimal perturbation can be required to obey. The gain obtained in this way is smaller than the previous ones (figure 16), but is still higher, at $Re = 1000$, than the Reynolds-number-independent case (solid line – \blacktriangle), which represents the lower limit for the gain.

The conclusion is therefore that the values of the gain are bounded between the free optimization results (upper limit) and the Reynolds-number-independent ones (lower limit). Any constraint on the initial perturbation produces an energy gain that is within these limits.

Many choices are available to constrain the initial perturbation to be zero on the wall. Among those, we assume $u_{\text{in}} = 0$ and $T_{\text{in}} = 0$ (in the compressible case). This is more consistent with the scaling adopted in §2, according to which the leading mechanism is associated with the lift-up effect in the presence of streamwise vortices. Due to this choice, all results presented in §6 refer to partial energy norm at the inlet (PENI), as defined in expression (3.5).

From this analysis it is clear that the iterative algorithm described in §3.3 and proposed as an efficient way to solve two coupled problems, which should be solved simultaneously, suffers some limitations at finite Reynolds number. The shortcoming is related to the choice of the energy norms, which change the coupling conditions at the inlet and/or outlet and therefore the solution of the complete optimization problem. When energy norms are those employed by Tumin & Reshotko (2003) (i.e. PENI and PENO – the extension to the compressible regime of the norms proposed by Luchini (2000) for the incompressible case), which are Reynolds-number independent, the convergence of the iterative procedure on the attractor is fast and usually does not require more than three forth–back iterations. On the other hand, the use of the full energy norm at the outlet and the partial one at the inlet (FENO and PENI), for $Re = 1000$, renders the convergence slower, requiring from five to ten iterations. If Reynolds number is increased so as to emulate the $Re \rightarrow \infty$ limit (e.g. $Re = 10^9$) results collapse onto the Reynolds-number-independent ones, as observed by Andersson *et al.* (1999) in the incompressible case, and convergence is fast. Several iterations are still required at $Re = 1000$ when the full energy norm is employed at both inlet and outlet (FENI and FENO), whereas a fast convergence is restored by smoothing the optimal perturbation at the inlet so as to avoid the discontinuity at $x = 0$, as discussed above. This smoothing, however, is arbitrary and does not guarantee a solution independent of its choice.

The fact that the algorithm relies on the existence of an attractor, which changes depending on the choice of the norm because the latter directly affects the initial conditions of the direct and/or adjoint problems, raises the question of a more robust optimization algorithm.

8. Conclusions

Optimal perturbations in the compressible regime have been considered for both a flat plate and a sphere. An adjoint-based optimization technique is employed and the discrete costate problem is obtained from the discretized direct problem by applying the Lagrangian multipliers technique in the discrete framework. This simplifies the code, reduces the number of possible errors, and allows the automatic generation of coupling conditions at the inlet and outlet. The code has been verified against available results (Tumin & Reshotko 2003, 2004).

The main contributions of the present work are an analysis that includes the full energy norm at the outlet and the fully discrete approach (including the coupling conditions), which considerably facilitates its implementation.

In the incompressible limit and for the flat plate (for which comparisons with the full energy norm at both inlet and outlet are available) it is found that the values of the gain are bounded by the free optimization results (the upper limit) and the Reynolds-number-independent ones (the lower limit). Any constraint on the initial perturbation produces an energy gain that is within these limits.

The norm to be maximized at the outlet, in the compressible case, is extended to the complete Mack's norm, including not only u_{out} and T_{out} in the fashion proposed by Luchini (2000) but also v_{out} and w_{out} .

Results for the flat plate show that when the Reynolds number is of the order of 10^3 , a significant difference in the energy growth (up to 17%) is found between the two choices of the outlet energy norm (full or partial). This is particularly true for supersonic values of the Mach number. On the other hand, when compressible effects are considerable but the basic flow is subsonic, the difference between the full and partial energy norms is not a critical factor. If the Reynolds number is greater than 10^4 , v_{out} and w_{out} do not play a significant role even in supersonic flows.

Results for the sphere are presented first by considering the use of the partial energy norm only and secondly by comparing them with the full energy norm, in the most interesting case. The effect of the wall temperature is in agreement with previous findings based on the parallel-flow model with curvature effects (Tumin & Reshotko 2001) and on the non-parallel flow model over a flat plate (Tumin & Reshotko 2003). In particular, the cooling of the wall destabilizes the flow with respect to the transient growth, with a difference up to two orders of magnitude when the adiabatic wall is compared to a cold wall ($T_w/T_{\text{ad}} = 0.25$). On the other hand, at fixed wall temperature, it is found that the energy growth is stronger in the proximity of the stagnation point, reinforcing what was found in the parallel-flow approximation. In contrast with the latter, however, the present model includes a significant feature, the divergence of the flow. In the parallel-flow approximation, the spanwise wavenumber β is a fixed parameter, whereas in this work the azimuthal index is kept constant so that the effective local spanwise wavenumber β is a function of the streamwise and radial coordinates. This divergence of the flow also leads to a modification of the energy norm resulting from the integration of the perturbation over a period in the azimuthal direction. Due to the scaling, the equations governing the perturbations on the sphere are not Reynolds-number independent. This reflects the twofold role of the radius of the sphere in the transient growth phenomenon. Not only does it enter the disturbance equations as the curvature parameter, but also the Reynolds number through the small parameter ϵ . The overall effect is an increase of the energy growth with the sphere radius. The use of the full energy norm at the outlet was also investigated. This was done close to the stagnation point and for a small range of the meridional angle, since this is the region where the largest gain is observed for the sphere in the case of the partial energy norm. Results reveal that, in the range of interesting values of Re_{ref} (related to the small parameter $\epsilon = (Re_{\text{ref}})^{-1/2}$) that are typical of wind tunnel tests or flight conditions, no significant role is played by v and w at the outlet. Despite the progress made in the present paper towards a better understanding of transient growth on blunt (spherical) noses, the ultimate elucidation of the blunt-body paradox would require solving the receptivity problem, which would explain the origin of the perturbation. This issue will be addressed in a future work.

This work was supported by the US Air Force Office of Scientific Research.

Appendix A. Matrices for compressible flow past a sphere

Assuming that the basic flow is known, let r , θ and ϕ denote respectively the radial, meridional and azimuthal coordinate and v , u , w be the corresponding velocity field. Temperature T and pressure p are the other unknowns of the problem, while density

ρ is related to T and p by the state equation and thus is not an explicit unknown. The radial coordinate $r = R + y$ includes the sphere radius R and the distance from the sphere surface y .

The scaling is as described in §2. There are only five unknowns in the disturbance equations and they are assumed to be proportional to $\exp(im\phi)$, where m is the azimuthal index and i the imaginary unit.

The scaling adopted for the sphere leads to the following relationships between ρ , p and T (the subscript S denotes basic flow), which allow us to recast the equations in five variables only:

$$\rho = -\frac{\rho_s T}{T_s}, \quad \rho_s = \frac{p_s}{T_s}.$$

In what follows viscosity μ_s is assumed to be a function of temperature only, and therefore μ'_s stands for the derivative $d\mu_s/dT_s$.

Transformations of the linearized equations lead to a system of partial differential equations

$$(\mathbf{A}f)_\theta = \mathbf{D}f_{\theta\eta} + \mathbf{B}_0f + \mathbf{B}_1f_\eta + \mathbf{B}_2f_{\eta\eta}, \quad (\text{A } 1)$$

where \mathbf{A} , \mathbf{B}_0 , \mathbf{B}_1 , \mathbf{B}_2 and \mathbf{D} are 5×5 matrices and $\eta = y/H_{\text{ref}}$ is the normalized distance from the wall. System (A 1) can be recast as

$$(\mathbf{H}_1f)_\theta + \mathbf{H}_2f = 0, \quad (\text{A } 2)$$

where the parabolic dependence on θ should be more clear and operators \mathbf{H}_1 and \mathbf{H}_2 are still 5×5 matrices and contain the dependence on θ and η :

$$\mathbf{H}_1 = \mathbf{A} - \mathbf{D}(\cdot)_\eta, \quad \mathbf{H}_2 = -\mathbf{B}_0 - [\mathbf{B}_1 - \mathbf{D}_\theta](\cdot)_\eta - \mathbf{B}_2(\cdot)_{\eta\eta}. \quad (\text{A } 3)$$

It should be noted that system (A 1) is written in a different form to (2.1). However, by rearranging the matrices, the same final forms (A 2) and (2.4) are obtained.

The expression to be maximized is the integral in the wall-normal direction of the kinetic energy and temperature

$$E_{\text{out}} = \int_0^\infty (1 + \epsilon\eta) \sin(\theta_{\text{out}}) \left[\rho_{s,\text{out}} [u_{\text{out}}^2 + \epsilon^2 (v_{\text{out}}^2 + w_{\text{out}}^2)] + \frac{p_{s,\text{out}} T_{\text{out}}^2}{(\gamma - 1) T_s^2 M^2} \right] d\eta, \quad (\text{A } 4)$$

where the term $(1 + \epsilon\eta) \sin(\theta_{\text{out}})$ comes from the integration over the whole domain, i.e. over the three independent variables.

The non-zero elements of the matrices are reported here. It should be noted that, formally, in the limit $\epsilon \rightarrow 0$, the geometric factor $(1 + \epsilon\eta)$ reduces to 1 and thus is automatically excluded from the denominator. The dependence on ϵ remains only in the terms associated with the centrifugal force such as B_0^{31} . However, in the present numerical implementation, the outer boundary η_{max} had to be chosen far away (of the order of 100) and $\epsilon = O(10^{-3})$, leading to $\epsilon\eta = O(10^{-1})$. Since $\epsilon\eta$ is not negligible, we keep the factor $(1 + \epsilon\eta)$ in the governing equations.

The wavenumber β in the following terms is defined as $\beta = m\epsilon / [(1 + \epsilon\eta) \sin \theta]$.

Continuity equation:

$$\begin{aligned} A^{11} &= \frac{\rho_s}{(1 + \epsilon\eta)}, & A^{14} &= -\frac{\rho_s U_s}{T_s(1 + \epsilon\eta)}, \\ B_0^{11} &= -\frac{\rho_s \cot \theta}{(1 + \epsilon\eta)}, & B_0^{12} &= -\frac{\partial \rho_s}{\partial \eta}, & B_0^{13} &= -\beta \rho_s, \\ B_0^{14} &= \frac{\partial}{\partial \eta} \left(\frac{\rho_s V_s}{T_s} \right) + \frac{\rho_s U_s \cot \theta}{T_s(1 + \epsilon\eta)}, & B_1^{12} &= -\rho_s, & B_1^{14} &= \frac{\rho_s V_s}{T_s}. \end{aligned}$$

θ -momentum equation:

$$\begin{aligned}
 A^{21} &= \frac{2\rho_s U_s}{(1+\epsilon\eta)}, & A^{24} &= -\frac{\rho_s U_s^2}{T_s(1+\epsilon\eta)}, \\
 B_0^{21} &= -\frac{\partial\rho_s V_s}{\partial\eta} - \mu_s \beta^2 - \frac{2\rho_s U_s \cot\theta}{(1+\epsilon\eta)}, & B_0^{22} &= -\frac{\partial\rho_s U_s}{\partial\eta}, & B_0^{23} &= -\beta\rho_s U_s, \\
 B_0^{24} &= \frac{\partial}{\partial\eta} \left(\frac{\rho_s V_s U_s}{T_s} \right) + \frac{\partial}{\partial\eta} \left(\mu'_s \frac{\partial U_s}{\partial\eta} \right) + \frac{\rho_s U_s^2 \cot\theta}{T_s(1+\epsilon\eta)}, & B_1^{21} &= \frac{\partial\mu_s}{\partial\eta} - \rho_s V_s, \\
 B_1^{22} &= -\rho_s U_s, & B_1^{24} &= \frac{\rho_s U_s V_s}{T_s} + \mu'_s \frac{\partial U_s}{\partial\eta}, & B_2^{21} &= \mu_s.
 \end{aligned}$$

r -momentum equation:

$$\begin{aligned}
 A^{31} &= \frac{\rho_s V_s}{(1+\epsilon\eta)} + \frac{2}{3(1+\epsilon\eta)} \frac{\partial\mu_s}{\partial\eta}, & A^{32} &= \frac{\rho_s U_s}{(1+\epsilon\eta)}, \\
 A^{34} &= -\frac{\rho_s U_s V_s}{T_s(1+\epsilon\eta)} - \frac{\mu'_s}{(1+\epsilon\eta)} \frac{\partial U_s}{\partial\eta}, \\
 B_0^{31} &= \frac{2}{3(1+\epsilon\eta)} \frac{\partial^2 \mu_s}{\partial\eta \partial\theta} - \frac{\rho_s V_s \cot\theta}{(1+\epsilon\eta)} + \frac{2\rho_s U_s}{\epsilon(1+\epsilon\eta)} - \frac{2 \cot\theta}{3(1+\epsilon\eta)} \frac{\partial\mu_s}{\partial\eta}, \\
 B_0^{32} &= -2 \frac{\partial\rho_s V_s}{\partial\eta} - \beta^2 \mu_s - \frac{\rho_s U_s \cot\theta}{(1+\epsilon\eta)}, & B_0^{33} &= -\beta\rho_s V_s - \frac{2\beta}{3} \frac{\partial\mu_s}{\partial\eta}, \\
 B_0^{34} &= \frac{2\rho_s V_s}{T_s} \frac{\partial V_s}{\partial\eta} + \frac{\partial\mu'_s}{\partial\eta} \left[\frac{4}{3} \frac{\partial V_s}{\partial\eta} - \frac{2}{3(1+\epsilon\eta) \sin\theta} \frac{\partial U_s \sin\theta}{\partial\theta} \right] \\
 &\quad + \mu'_s \frac{\partial}{\partial\eta} \left(\frac{4}{3} \frac{\partial V_s}{\partial\eta} - \frac{2}{3(1+\epsilon\eta) \sin\theta} \frac{\partial U_s \sin\theta}{\partial\theta} \right) + V_s^2 \frac{\partial}{\partial\eta} \left(\frac{\rho_s}{T_s} \right) \\
 &\quad + \frac{\rho_s U_s V_s \cot\theta}{T_s(1+\epsilon\eta)} - \frac{\rho_s U_s^2}{\epsilon T_s(1+\epsilon\eta)} + \frac{\mu'_s \cot\theta}{(1+\epsilon\eta)} \frac{\partial U_s}{\partial\eta}, \\
 B_1^{31} &= \frac{1}{(1+\epsilon\eta)} \frac{\partial\mu_s}{\partial\theta} + \frac{\mu_s \cot\theta}{3(1+\epsilon\eta)}, & B_1^{32} &= -2\rho_s V_s + \frac{4}{3} \frac{\partial\mu_s}{\partial\eta}, \\
 B_1^{33} &= \frac{\beta\mu_s}{3(1+\epsilon\eta)}, & B_1^{34} &= \mu'_s \left[\frac{4}{3} \frac{\partial V_s}{\partial\eta} - \frac{2}{3(1+\epsilon\eta) \sin\theta} \frac{\partial U_s \sin\theta}{\partial\theta} \right] + \frac{\rho_s V_s^2}{T_s} \\
 B_1^{35} &= -1, & B_2^{32} &= \frac{4}{3} \mu_s, \\
 D^{31} &= \frac{\mu_s}{3(1+\epsilon\eta)}.
 \end{aligned}$$

ϕ -momentum equation:

$$\begin{aligned}
 A^{43} &= \frac{\rho_s U_s}{(1+\epsilon\eta)}, & A^{44} &= \frac{\mu_s \beta U_s}{3T_s(1+\epsilon\eta)}, \\
 B_0^{41} &= \frac{\mu_s \beta}{3\rho_s(1+\epsilon\eta)} \frac{\partial\rho_s}{\partial\theta} - \frac{\beta}{(1+\epsilon\eta)} \frac{\partial\mu_s}{\partial\theta} - \frac{2\beta\mu_s \cot\theta}{(1+\epsilon\eta)}, & B_0^{42} &= \frac{\mu_s \beta}{3\rho_s} \frac{\partial\rho_s}{\partial\eta} - \beta \frac{\partial\mu_s}{\partial\eta}, \\
 B_0^{43} &= -\beta^2 \mu_s - \frac{\partial\rho_s V_s}{\partial\eta} - \frac{2\rho_s U_s \cot\theta}{(1+\epsilon\eta)},
 \end{aligned}$$

$$B_0^{44} = \frac{\rho_s U_s \beta}{3T_s(1 + \epsilon\eta)} \frac{\partial}{\partial \theta} \left(\frac{\mu_s}{\rho_s} \right) - \frac{2\mu'_s \beta U_s \cot \theta}{(1 + \epsilon\eta)}$$

$$+ \mu'_s \frac{2\beta}{3} \left[\frac{\partial V_s}{\partial \eta} + \frac{1}{(1 + \epsilon\eta) \sin \theta} \frac{\partial}{\partial \theta} (U_s \sin \theta) \right] - \frac{\mu_s \beta}{3\rho_s} \frac{\partial}{\partial \eta} \left(\frac{\rho_s V_s}{T_s} \right) - \frac{\mu_s \beta U_s \cot \theta}{3T_s(1 + \epsilon\eta)},$$

$$B_0^{45} = \beta, \quad B_1^{43} = -\rho_s V_s + \frac{\partial \mu_s}{\partial \eta}, \quad B_1^{44} = -\frac{\beta \mu_s V_s}{3T_s}, \quad B_2^{43} = \mu_s.$$

Energy equation:

$$A^{51} = \frac{\rho_s T_s}{(1 + \epsilon\eta)},$$

$$B_0^{51} = \frac{\gamma - 1}{\gamma(1 + \epsilon\eta)} \frac{\partial p_s}{\partial \theta} - \frac{\rho_s T_s \cot \theta}{(1 + \epsilon\eta)}, \quad B_0^{53} = -\beta \rho_s T_s,$$

$$B_0^{54} = \mu'_s (\gamma - 1) M_{\text{ref}}^2 \left(\frac{\partial U_s}{\partial \eta} \right)^2 - \frac{\beta^2 \mu_s}{Pr} + \frac{1}{Pr} \frac{\partial}{\partial \eta} \left(\mu'_s \frac{\partial T_s}{\partial \eta} \right),$$

$$B_1^{51} = 2(\gamma - 1) M_{\text{ref}}^2 \mu_s \frac{\partial U_s}{\partial \eta}, \quad B_1^{52} = -\rho_s T_s, \quad B_1^{54} = \frac{2}{Pr} \frac{\partial \mu_s}{\partial \eta},$$

$$B_2^{54} = \frac{\mu_s}{Pr}.$$

REFERENCES

- ANDERSON, J. D. 2000 *Hypersonic and High Temperature Gas Dynamics*. AIAA.
- ANDERSSON, P., BERGGREN, M. & HENNINGSON, D. S. 1999 Optimal disturbances and bypass transition in boundary layers. *Phys. Fluids* **11**, 134–150.
- BENNEY, D. J. & GUSTAVSSON, L. H. 1981 A new mechanism for linear and nonlinear hydrodynamic instability. *Stud. Appl. Maths* **64**, 185–209.
- BOBERG, L. & BROSIA, U. 1988 Onset of turbulence in a pipe. *Z. Naturforschung* **43a**, 697–726.
- BUTLER, K. M. & FARRELL, B. 1992 Three-dimensional optimal perturbations in viscous shear flow. *Phys. Fluids A* **4**, 1637–1650.
- CATHALIFAUD, P. & LUCHINI, P. 2000 Algebraic growth in boundary layers: optimal control by blowing and suction at the wall. *Eur. J. Mech. B/Fluids* **19**, 469–490.
- ELLINGSEN, T. & PALM, E. 1975 Stability of linear flow. *Phys. Fluids* **18**, 487–488.
- FARRELL, B. 1982 The initial growth of disturbances in a baroclinic flow. *J. Atmos. Sci.* **39**, 1663–1686.
- FARRELL, B. 1984 Modal and non-modal baroclinic waves. *J. Atmos. Sci.* **41**, 668–673.
- FARRELL, B. 1986 Transient growth of damped baroclinic waves. *J. Atmos. Sci.* **42**, 2718–2727.
- FARRELL, B. 1987 Developing disturbances in shear. *J. Atmos. Sci.* **44**, 2191–2199.
- FARRELL, B. 1988a Optimal excitation of neutral Rossby waves. *J. Atmos. Sci.* **45**, 163–172.
- FARRELL, B. 1988b Optimal excitation of perturbations in viscous shear flow. *Phys. Fluids* **31**, 2093–2102.
- FARRELL, B. F. & MOORE, A. M. 1992 An adjoint method for obtaining the most rapidly growing perturbation to oceanic flows. *J. Phys. Oceanogr.* **22**, 338–349.
- GUNZBURGER, M. 2000 Adjoint equation-based methods for control problems in incompressible, viscous flows. *Flow, Turb. Combust* **65**, 249–272.
- GUSTAVSSON, L. H. 1981 Resonant growth of three-dimensional disturbances in plane Poiseuille flow. *J. Fluid Mech.* **112**, 253–264.
- GUSTAVSSON, L. H. 1991 Energy growth of three-dimensional disturbances in plane Poiseuille flow. *J. Fluid Mech.* **224**, 241–260.
- GUSTAVSSON, L. H. & HULTGREN, L. S. 1980 A resonance mechanism in plane Couette flow. *J. Fluid Mech.* **98**, 149–159.

- HANIFI, A. & HENNINGSON, D. 1998 The compressible inviscid algebraic instability for streamwise independent disturbances. *Phys. Fluids* **10**, 1784–1786.
- HANIFI, A., SCHMIDT, P. J. & HENNINGSON, D. 1996 Transient growth in compressible boundary layer flow. *Phys. Fluids* **8**, 51–65.
- HULTGREN, L. S. & GUSTAVSSON, L. H. 1981 Algebraic growth of disturbances in a laminar boundary layer. *Phys. Fluids* **24**, 1000–1004.
- JANG, P. S., BENNEY, D. J. & GRAN, R. L. 1986 On the origin of streamwise vortices in a turbulent boundary layer. *J. Fluid Mech.* **169**, 109–123.
- KREYSZIG, E. 1989 *Introductory Functional Analysis with Applications*. John Wiley & Sons.
- LANDAHL, M. T. 1975 Wave breakdown and turbulence. *SIAM J. Appl. Maths* **28**, 735–756.
- LANDAHL, M. T. 1980 A note on an algebraic instability of inviscid parallel shear flow. *J. Fluid Mech.* **98**, 243–251.
- LUCHINI, P. 2000 Reynolds–number–independent instability of the boundary layer over a flat surface: optimal perturbations. *J. Fluid Mech.* **404**, 289–309.
- LUCHINI, P. & BOTTARO, A. 1998 Görtler vortices: a backward–in–time approach to the receptivity problem. *J. Fluid Mech.* **363**, 1–23.
- LUCHINI, P. & BOTTARO, A. 2001 Linear stability and receptivity analyses of the Stokes layer produced by an impulsively started plate. *Phys. Fluids* **13**, 1668–1678.
- MACK, L. M. 1969 Boundary layer stability theory. *JPL Rep.* 900-277. Jet Propulsion Lab., California Institute of Technology, Pasadena, CA, USA.
- NAYLOR, A. W. & SELL, G. R. 2000 *Linear Operator Theory in Engineering and Science*. Springer.
- REDDY, S. C. & HENNINGSON, D. S. 1993 Energy growth in viscous channel flows. *J. Fluid Mech.* **252**, 209–238.
- RESHOTKO, E. 2001 Transient growth: a factor in bypass transition. *Phys. Fluids* **13**, 1067–1075.
- RESHOTKO, E. & TUMIN, A. 2000 The blunt body paradox – a case for transient growth. In *Laminar–Turbulent Transition* (ed. H. F. Fasel & W. S. Saric), pp. 403–408. Springer.
- RESHOTKO, E. & TUMIN, A. 2004 The role of transient growth in roughness-induced transition. *AIAA J.* **42**, 766–770.
- SCHMID, P. J. & HENNINGSON, D. S. 2001 *Stability and Transition in Shear Flows*. Springer.
- TING, L. 1965 On the initial conditions for boundary layer equations. *J. Math. Phys.* **44**, 353–367.
- TREFETHEN, L. N., TREFETHEN, A. E., REDDY, S. C. & DRISCOLL, T. A. 1993 Hydrodynamic stability without eigenvalues. *Science* **261**, 578–584.
- TUMIN, A. & RESHOTKO, E. 2001 Spatial theory of optimal disturbances in boundary layers. *Phys. Fluids* **13**, 2097–2104.
- TUMIN, A. & RESHOTKO, E. 2003 Optimal disturbances in compressible boundary layers. *AIAA J.* **41**, 2357–2363.
- TUMIN, A. & RESHOTKO, E. 2004 Optimal disturbances in the boundary layer over a sphere. *AIAA Paper* 2004–2241.
- ZUCCHER, S., BOTTARO, A. & LUCHINI, P. 2006 Algebraic growth in a blasius boundary layer: Nonlinear optimal disturbances. *Eur. J. Mech. B/Fluids* **25**, 1–17.
- ZUCCHER, S., LUCHINI, P. & BOTTARO, A. 2004 Algebraic growth in a Blasius boundary layer: Optimal and robust control by mean suction in the nonlinear regime. *J. Fluid Mech.* **513**, 135–160.